Numerical Study of Crack Propagation in Boulders Subjected to Diurnal Solar Irradiation

Smit Kamal

A thesis
submitted in partial fulfillment of the
requirements for the degree of

Master of Science in Civil Engineering

University of Washington

2018

Reading Committee:

Peter Mackenzie-Helnwein, Co-Chair

Bernard Hallet, Co-Chair

Richard Wiebe

Program Authorized to Offer Degree:
Civil and Environmental Engineering

University of Washington

Abstract

Numerical Study of Crack Propagation in Boulders Subjected to Diurnal Solar Irradiation

Smit Kamal

Co-Chairs of the Supervisory Committee:
Research Associate Professor Peter Mackenzie-Helnwein
Department of Civil and Environmental Engineering

Professor Bernard Hallet
Department of Earth and Space Sciences and Qaternary Research Center

Considerable evidence from field observations and measurements suggests that thermal stresses induced by daily exposure to the sun contribute significantly to mechanical weathering, the breakdown of rocks at the ground surface (Mcfadden et al. 2005; Aldred et al. 2016; Eppes et al. 2016). A solid theoretical foundation for quantifying and understanding these stresses is, however, currently lacking. We develop it using a 3d finite element (FE) model, coupling radiation and conduction with elastic response, to compute the time-varying stress state in mechanically isotropic, homogenous boulders exposed to the sun on Earth. As crack growth in brittle materials are generally dominated by tensile stresses, we focus on the temporal relationship between temperature and solar induced tensile stresses at a macroscopic level in distinct regions of boulders of different sizes. We found significant temporal variation in the magnitude, location, and spatial extent of elevated tensile stresses.

Since fracture in brittle materials generally initiates from pre-existing defects, which are widely distributed through most materials (Danzer et al. 2007), the strength of a specimen is strongly affected by its size. To assess how the interaction of time varying tensile stresses with pre-existing defects in surface boulders affects their resistance to thermal breakdown, we carried out a probabilistic study. Using the Weibull theory, we calculated the probability of crack growth caused solely by diurnal solar exposure in boulders of different size. Our numerical results illuminate the complex size-dependent thermo-mechanical behavior. Interestingly, they suggest that solar induced stresses for 0.3 m-diameter boulder are most likely to initiate crack growth between 4:00 pm to 6:00 pm, which is consistent with the field measurements of acoustic emissions that are only available for this boulder size (Eppes et al. 2016).

TABLE OF CONTENTS

LIST OF FIGURES

LIST OF TABLES

ACKNOWLEDGMENTS

This thesis is probably the best thing I have got a chance to work on and I would like to express my gratitude to everyone who made this happen. Thank you Professor Peter Mackenzie-Helnwein and Professor Bernard Hallet for giving me this amazing opportunity and for never giving up on me whenever I messed up. I'm really grateful for the teachings and love I received from both of you. Every bit of this research was possible becasue of your efforts. I am thankful to Professor Richard Wiebe for his time and valuable feedbacks on this thesis.

I would not have been able to do this project without the support and love of my parents. Thank you for constantly pushing me to go for the things I like and for picking me up whenever I was down. I would also love to thank all my friends who kept me going during difficult times and whose presence made me feel a lot stronger. Thank you Carina, Revathi, Naman, Siddharth, Tom, Nate, Gabby, Spencer, Raktim, Chirag, Raunaq, Adheesh, Avinash, and Arya.

This work was supported by NASA through sub-contract #12-0233 from Malin Space Science Systems from their contract with Jet Propulsion Laboratory Contract #1516826 for Mars Science Laboratory Mastcam, MARDI, and MAHLI Science and Operations.

DEDICATION

Dedicated to my parents and my master's thesis advisors.

Chapter 1

INTRODUCTION

1.1 Prologue

"Physical weathering is the disaggregation of rocks into smaller pieces without any changes in their chemistry or mineralogy" (Thomas et al. 2005), while "chemical weathering is the process by which mineral or rock is dissolved, oxidized, or reduced, and transformed to secondary products that are stable" (Yokoyama and Matsukura 2006). Physical and chemical weathering affect each other and are subsequently responsible for erosion (Thomas et al. 2005; Yokoyama and Matsukura 2006). Therefore, a thorough understanding of different physical weathering processes and their interactions is fundamental in studies of landscape evolution in diverse settings on Earth and other planets. Recent field observations and measurements (Mcfadden et al. 2005; Eppes et al. 2015, 2016) suggest that solar induced thermal stresses are responsible for cracks on boulders of Earth and Mars. However, a firm theoretical foundation is lacking for quantifying the stress field in such boulders and the link between solar induced thermal stresses and the preferred orientation of cracks observed on boulders of Earth and Mars. This research presented herein seeks to quantify the stress state and the probability of crack growth in boulders with a focus on the influence of boulder size. Thomas et al. 2005, using the available imagery from NASA's 'Spirit' and 'Opportunity' rovers, suggested that many of the weathering features of Mars appear to have formed by processes similar on Earth, and could be explained without considering any extraterrestrial processes. Because of the similarity in geometric insolation of Earth and Mars, the spatial distribution of solar induced thermal stresses in boulders of Earth and Mars can expected to be similar (Eppes et al. 2015). Considering this similarity, the implications of our study extend beyond Earth to Mars. We have studied the time varying mechanical and thermal response of spherical boulders of different sizes that are subjected to diurnal solar cycles. The probability of crack growth in boulders of different sizes at different times during a typical day has been analyzed

based on the concepts developed by Weibull 1939.

1.2 Literature review

Physical weathering significantly influences sediment production, rock erosion and chemical weathering (Eppes et al. 2015). Deducing the origin of fractures in boulders can help us understand the influence of individual mechanical weathering processes and their interaction, which can be a key in understanding landscape evolution.

The potential role of solar induced thermal stresses in rock cracking on Earth has received considerable attention (Griggs 1936; Mcfadden et al. 2005). However, Griggs 1936 casted lasting doubt on the importance of these thermal stresses in rock breakdown with his experimental results. In his experiment, he subjected small tablets a Minnesota Pink Granite with dimensions $3\frac{1}{4}$ inch$\times$ $3\frac{1}{4}$ inch $\times$ $2\frac{3}{4}$ inch (80 mm $\times$ 80 mm $\times$ 70 mm) to artificial temperature changes in 15 minutes cycles (5 minutes of heating and 10 minutes of cooling) varying from 32 °C to 142 °C. He carefully minimized potential effects of hydration and freezing by using radiant heat, dry cooling, and maintaining temperature above 0 °C. The tablets were subjected to 89,400 cycles of this experiments, equivalent to 244 years of diurnal temperature change to examine the effect of fatigue by insolation. Griggs estimated that a large difference in surface-parallel stress exists which caused shear stress in the experiments about twenty-one times as great as those produced in granite outcrops subjected to diurnal temperature change of 60 °C. However, the photomicrographs of the surface before and after the experiment showed no change. This experiment concluded that diurnal temperature changes over a large period of time is insufficient to cause any ex-foliation or disintegration of granite.

In the decades after the experiments of Griggs 1936 interest in solar-induced rock breakdown dwindled until Mcfadden et al. 2005 suggested that diurnal stresses induced by the sun could initiate cracks in boulders on Earth. They observed boulders at eight sites in mid latitude deserts and characterized four different type of cracks, ie. longitudinal, surface parallel, fabric related, and meridional. The azimuth (the strike) of meridional cracks preferentially aligned north-south, and crack width and length appeared to increase with time, indicating an evolutionary sequence or crack development. The authors hypothesized that

steeply dipping north-south cracks occurred because of thermal stresses produced by the recurrent directional diurnal heating and cooling of the clasts surface. The paper suggested that in subareal environments at midday, when the tendency for the outer shell of a clast to expand was greatest relative to its cooler interior, internal tension peaked, and vertical cracks initiated in the interior of the clast and eventually propagated to the surface; the daily movement of the sun introduced asymmetrical stresses, which favored the growth of cracks perpendicular to its track. They also proposed that, following sunrise, the region of maximum surface heating of an equidimensional clast progressed in an east-west direction across the clast surface and internal tensile stresses increased as the rock surface warms and heat penetrates in the interior throughout morning. The authors hypothesized that elevated tensile stresses were near horizontal and oriented roughly east west, favoring near vertical cracks striking north-south.

Eppes et al. 2016 carried out a study of individual mechanical weathering processes and their interactions. They presented an eleven-month data set of crack growth, monitored using Acoustic Emissions (AE), combined with measurements of rock surface temperature and strain, and environmental conditions, recorded continuously for a granite boulder resting on ground in open sun. The authors also carried out a finite element analysis of a spherical boulder subjected to diurnal cycles in order to define the temperature and macroscopic stress distribution in the boulder. Crack growth observed from AEs did not correlate with temperature, temperature range, rate of temperature change, wind speed, precipitation or freezing. A consistent characteristic of all crack activity observed by AEs is their occurrence during periods when thermally induced tensile stresses peaked according to the finite element model of thermal stresses during simple diurnal solar exposure. This lead the authors to suggest that solar-induced thermal stresses due to simple diurnal forcing are sufficient to initiate sub-critical crack growth and elevate the tensile stress field which makes the rock susceptible to cracking triggered by other weathering mechanisms.

"Mechanical weathering data from extraterrestrial rocks which might support, refute or quantify the relative importance of different mechanical weathering processes have not been collected" (Eppes et al. 2016). They obtained orientation measurements of 1857 cracks visible in 1573 rocks along the Spirit (Mars Rover) traverse and observed that the cracks were ori-

ented in statistically preferred directions similar to those observed on Earth in mid-latitude deserts Mcfadden et al. 2005. Citing the similarity in geometry of insolation between Earth and Mars because of their analogs long term orbit cycles, the authors suggested solar-induced thermal stresses as the source of cracks having preferred orientation on Martian boulders. The authors used a 2-D finite element-model of a micro-structure subjected to diurnal thermal forcing, to simulate solar induced thermal stress that can develop at the grain scale in polycrystalline rock on Martian surface, and found the peak tensile and compressive stresses of 12 and 17 MPa, respectively. They noted that these stresses are of similar order of magnitude to macroscopic tensile stress of the rocks and within 80% limit for sub-critical crack growth. This added support to the notion of diurnal thermal stresses initiating cracks on Martian Rocks. The authors also found significant differences in preferred crack orientation between Martian boulders and Earth boulders. The strikes of cracks on Martian boulders were generally East-West with a large variance compared to the more distinct preferred North-South direction on Earth. The authors believed that the difference in obliquity of Earth and Mars, along with the differences in latitude, longitude, altitude, topographical shading, rock composition, and shape of boulders of Earth and Mars, could account for the differences in crack orientation. The authors also hypothesized that the relatively large variance in strike of Martian boulders could reflect the influence of additional weathering processes. The results of Eppes et al. 2016 highlight the need for a better understanding of the thermally induced stress state in boulders in diverse settings.

Shi 2011, for the first time, assessed the temporal evolution of the thermal and stress states at macroscopic level within boulders on Earth that are exposed to the sun. The research provided quantitative evidence showing that solar induced thermal stresses in boulders are sufficient to induce sub-critical crack growth in Earth boulders. This research however did not deal systematically with the important effects of boulder size, and probabilistic aspect of crack growth. Considering the limitations of these studies, we re-examine the hypothesis of solar induced thermal stresses driving cracks in surface rocks using 3d coupled thermo-mechanical finite element simulations of Earth boulders of different sizes subjected to diurnal solar cycles . We also explored how the time varying solar induced tensile stresses affect the likelihood of crack growth in boulders of different sizes based on the probabilistic

principles developed by Weibull 1939.

1.3 Research objectives

The two major objectives of this research are :

- Understand the temporal variation of the stress and temperature fields in boulders of different sizes because of diurnal solar exposure.

- Deduce the probability of crack growth in boulders of different sizes using the principles developed by Weibull 1939, based on the results from 3d coupled thermo-mechanical finite element simulations.

These findings illuminate the potential role of diurnal insolation in breaking down surface rocks and shaping landscapes on Earth and other planetary bodies. The tools and techniques developed for this research can also be used in other domains of structural engineering involving fracture, fatigue and thermal stresses.

1.4 Research development and procedure

The 3d coupled thermo-mechanical finite element models used in this study were derived from models developed by Shi 2011. The details about the finite element model development and its preliminary validation can thus be found in his thesis These models were modified for the present research as summarized in Section 2.2. The 3d coupled thermo-mechanical finite element simulations were carried out using MSC.marc 2015. The data obtained from these simulations were extracted and analyzed using Python to define the solar induced thermal stress state and the probability of crack growth in boulders of different size.

1.5 Thesis outline

Chapter 2 helps understand the time varying nature of boulder's temperature distribution due to diurnal cycles of solar exposure, and how it affects the stresses at the surface and interior of the boulder. It also sheds light on aspects of the problem that were not covered by Shi 2011 and notes the modifications made in Shi's model for the present research. The

3d distribution of tensile principal stress and temperature on the surface and various planes passing through the boulders are illustrated for times through the day when tensile principal stress in boulders reach peak values. The principal tensile stress at various distances relative to the skin depth are also presented for boulders of different sizes.

The 3d coupled thermo-mechanical finite element simulations shows quantitatively how the spatial distribution of principal tensile stress varies with boulder's size. This leads to Chapter 3, which addresses the probability of crack growth within different regions of boulders of different sizes, based on the time varying location, magnitude, and spatial extent of tensile principal stress.

Chapter 2

3D COUPLED THERMO-MECHANICAL FINITE ELEMENT SIMULATIONS

2.1 Introduction

Mcfadden et al. 2005 suggested that diurnal stresses induced by the sun have the ability to initiate cracks on the boulders of Earth due to the directional heating and cooling of the boulders. This suggestions gained support from Eppes et al. 2016, who recorded acoustic emission (AE) data for eleven months in a boulder to monitor crack growth along with environmental conditions. They reported that most events were detected from AEs during a period when thermally induced principal tensile stresses in rocks predicted by numerical models of Shi 2011 were highest.

Shi 2011 developed a 3d thermo-mechanical model in MSC.marc, to quantitatively investigate the temporal and spatial distribution of temperature and stress throughout the boulders due to diurnal insolation. The model accounted for the effect of direct sol radiation, atmospheric damping, secondary heat exchange with air, and transient heat conduction in both rock and soil, as well as the influence of geographical location and season. Effects of meteorological phenomena, such as rain and wind were not modeled. The thermal aspect of the model was verified and validated by comparing its thermal results with that of the field measurements made by Eppes et al. 2010. Shi 2011 simulated a series of spherical boulders made of granite, under weather conditions specific to January 14 , 2011 where the boulder in Eppes et al. 2010 was located at Redlair Preserve, Gaston County, North Carolina (35° 17' 55" N and 81° 5' 17" W).

As in this thesis, Shi 2011 assumed that crack growth in brittle materials is driven by Mode I failure due to tension; hence, the attention natually focuses on where and when during course of a day the maximum principal stress (tensile stresses being positive) develops in boulders of different sizes. He suggested that directional solar heating, on its own, was

sufficient to cause sub-critical crack growth in boulders, and concluded that for boulders with diameter greater that 1.5 m, cracks are more likely to grow near the surface where they experienced higher tensile stress, while for smaller boulders cracks are more likely to grow in the interior.

The model described herein extends, Shi's study through several improvements largely to eliminate limitations arising from the boulders of different sizes in Shi's study being scaled versions of each other, with similar mesh structure and simiar numbers of finite elements, and yet, the depth of heat penetration in these boulder would be the same at any given time as all boulders had the same material properties. This numerical complication, which has been circumvented herein, interfered with the systematic study of size effects.

This chapter is an extension of research carried out by Shi 2011 and paves way towards developing a deeper quantitative understanding of the thermal and structural response of boulders subjected to diurnal solar irradiation. It further illustrates and discusses the stress and temperature distribution throughout boulders of different sizes, with special focus on times when tensile stresses reach their peak on the surface and in the interior of boulders. The maximum principal stress observed at specific depths from the surface is also be presented.

2.2 Model development

This study used the validated thermo-mechanical finite element model developed by Shi 2011 in MSC.marc with modifications. The model consists of a boulder that rests on soil. The entire system is subjected to diurnal solar irradiation, while the soil is underlaid by a numerical radiation shield. Orthogonal axes were used as a reference frame for the finite

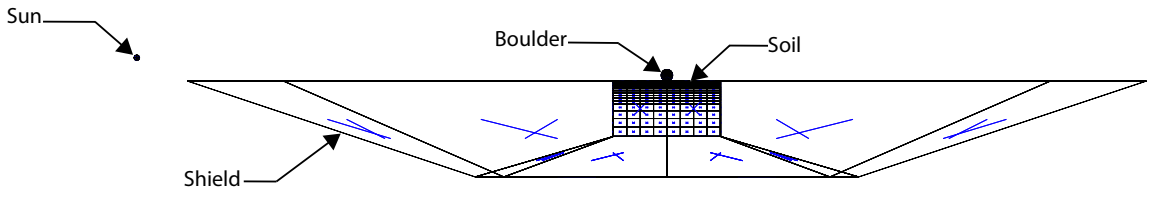

Figure 2.1: Finite element models used for study

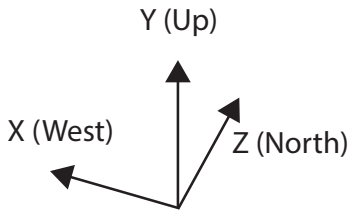

Figure 2.2: Reference frame used in finite element model

element models. The X axis of the co-ordinate system points towards the west, the Y axis points towards the sky, and the Z axis points north (2.2).

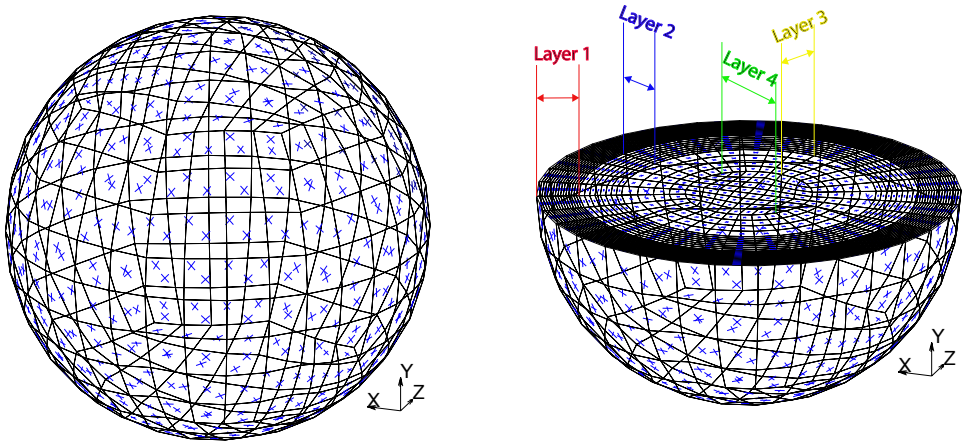

(a) **(b)**

Figure 2.3: Boulder's finite element model (a) complete boulder (b) bottom half of the boulder

The finite element model of the boulder comprises Hex(8) elements (eight node hexahedral element) of MSC.marc and is illustrated in Figure 2.3. The boulder consists of four major concentric layers (shells), each of which is made up of sub-layers of Hex(8) elements. The boundary of each layer is shown in Figure 2.3(b). Layer 1, 2 and 3 constitute of elements having the same thickness in the radial direction. The basic structure of all the boulders used in this study are same as illustrated in Figure 2.3 and they can be scaled to different

diameters. Layer 1 has the finest mesh while Layer 4 has the coarsest. Layer 1 and Layer 2 of different boulders were selectively refined to accurately model the effect of incoming insolation. The thickness of Layer 1 and Layer 2 of the boulders are equal to 0.2 times the radius of the boulder, Layer 3 has a thickness equal to 0.3 times the radius of the boulder, while the Layer 4 has a thickness equal to 0.3 times the radius of the boulder. Spherical boulders of diameters 0.150 m, 0.200 m, 0.250 m, 0.300 m, 0.500 m, 0.625 m, 0.750 m, 0.875 m, 1.000 m, 1.250 m, 1.500 m, 2.000 m, 3.000 m, and 5.000 m were analyzed in this research.

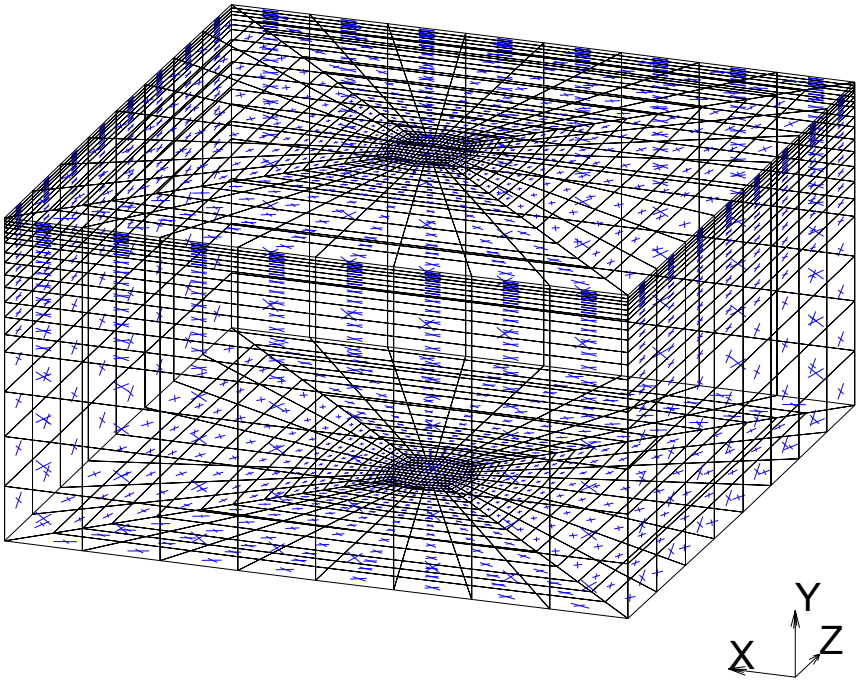

Figure 2.4: Soil used in the finite element model

The enlarged view of soil shown in Figure 2.1 is presented in Figure 2.4. The soil domain is a rectangular prism and made up of layers constituting of Hex(8) elements. The dimensions of soil was varied with boulder diameter in some cases. The coarseness of mesh was increased from the top layer to the base layer. The boulder lies on the centroid of the top horizontal surface of the soil and fineness of mesh increases with proximity to the boulder. Similar to

the boulder, the soil could be scaled to different dimensions.

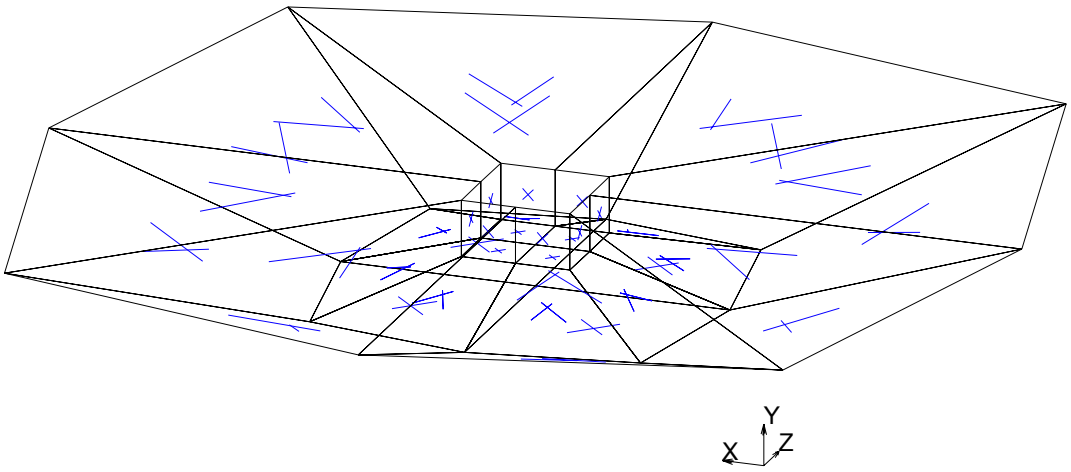

Figure 2.5: Shield used in finite element model

The shield used in the finite element model is shown in Figure 2.5. The shield is trapezoidal in shape and has a void which can fit the soil. The shield is also made up for Hex(8) elements and can be scaled to fit soil of different sizes. The shield was constructed to prevent the solar insolation from reaching the boulder prior to sunrise and after sunset.

The sun model used in the finite element model is illustrated in Figure 2.6. The sun moves in a diurnal manner along relative to the boulder, soil and shielded system. The sun is made up of eight Hex(8) elements. The heat flux from the sun to any given element will be unaltered if the ratio between sun's diameter to the distance of the sun from the element is kept constant (Shi 2011). Considering this fact, the radius of the sun model was varied to improve the computations pertaining to radiation such that the ratio between the sun model's diameter to distance between sun model and the boulder's model remained constant.

Further details pertaining to model development and validation can be found in Shi 2011. The following changes were made to Shi's model for the present study.

- The material properties of different constituents of the 3d coupled thermo mechanical finite element models used in this study are shown in Table 2.1.

- The thermal and mechanical response of boulders were analyzed once the boulders

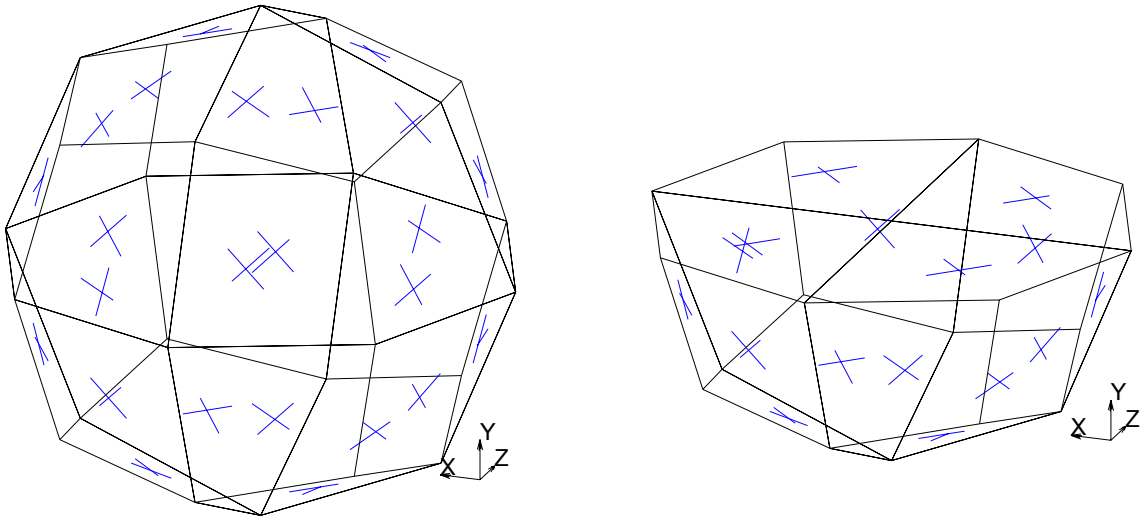

(a) **(b)**

Figure 2.6: Finite element model of the sun (a) complete sun (b) bottom half of the sun

reached a steady periodic state. The time taken by boulders to reach this state, commonly known as preconditioning time is in Table 2.2. The simulation for preconditioning phase was carried out with time increments of two hours.

- The thermal and structural response of boulders were analyzed and presented after the boulders reached a steady periodic state. The time taken by boulders to reach a steady periodic state has been referred to as preconditioning time and has been shown in Table 2.3. The simulation for preconditioning phase was carried out a time increment of two hours. Following the preconditioning phase, the boulders were simulated for one additional day of solar irradiation at a time increment of fifteen minutes. The structural and thermal response from the last day of simulation following the preconditioning phase are presented in this document.

- Tolerances for view factors , number of pixels , and size of the finite element model of the sun were varied with the boulder's diameter to accurately model the effect of radiation. The ratio of the sun's diameter to the distance from the boulder was kept constant such that the amount of insolation remained unaltered. Details pertaining to

Table 2.1: Material properties used in modeling

Property	Symbol	Boulder	Soil	Shield	Sun
Mass density	ρ (kg m^{-3})	2760	1600	1	1
Modulus of elasticity	E (MPa)	53000	75	210000	210000
Poisson's ratio	ν	0.28	0.35	0.25	0.25
Coefficient of Thermal expansion	α (K^{-1})	8.5×10^{-6}	1.25×10^{-5}	0	0
Emissivity	ϵ	0.45	0.65	0	1
Thermal conductivity	κ (J h^{-1} m^{-1} K^{-1})	9360	5400	0.036	3.6×10^6
Specific heat	c (J kg^{-1} K^{-1})	1000	750	10^9	1

view factors, number of pixels, and diameter of the finite element model of the sun are presented in Table 2.4.

- Similar to Shi's model, the preliminary finite element models were created by scaling a reference boulder to different diameters. Since heat penetrates to equal depth from the surface in the boulders irrespective of their sizes, mesh refinement was carried out such that the thickness of element along radial direction did not exceed 0.02 m in Layer 1 and 0.35 m elsewhere. Table 2.5 illustrates the thickness of elements in various layers of the boulders along the radial direction.

The simulations were carried out for winter solstice, December 21, at the study site in Redlair Preserve, Gaston County, North Carolina (35° 17' 55" N and 81° 5' 17" W). The sun rose and set in the simulations at 7:08 am and 4:52 pm respectively.

Table 2.2: Initial temperature at surface nodes

Boulder Diameter (m)	Boulder initial temperature (°C)	Soil initial temperature (°C)
0.150	-4	-4
0.200	-4	-4
0.250	-4	-4
0.300	-4	-4
0.500	1	-4
0.625	1	-4
0.750	1	-4
0.875	1	-4
1.000	1	-4
1.250	1	-4
1.500	1	1
2.000	1	-4
3.000	1	-4
5.000	4	-4

2.3 Thermal and structural response of the boulders

In this section we study the evolution of stress and temperature fields in boulder when tensile stresses (tension) reach their peak values at surface and in the interior. The key assumption of our study is that the crack growth in boulders is driven by tensile stresses. We illustrate model results for spherical boulders of diameters 0.30 m, 0.50 m, 1.00 m, 3.00 m, and 5.00 m, subjected to diurnal solar radiation as these boulders represent a wide range of surface rocks. We show the spatial distribution of maximum tension and temperature on the surface and along various planes passing through the boulders when maximum tension in boulders reach their peak magnitude at the surface and at the interior. The distribution of compressive

Table 2.3: Preconditioning time for different boulders

Boulder Diameter (m)	Preconditioning time
$\leq$ 1.000	2 days
1.250 and 1.500	7 days
2.000	14 days
3.000	21 days
5.000	42 days

stress will not be shown because it less significant; it is represented by dark gray in the figures. The simulations did not address actual crack growth in boulders.

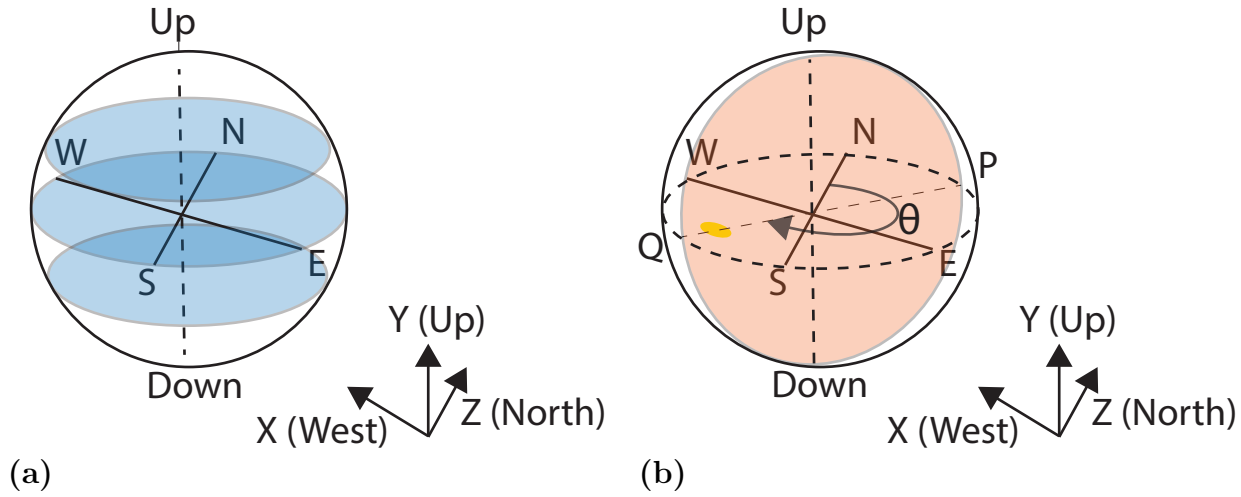

Figure 2.7: Cutting planes passing through the boulders: (a) Equidistant horizontal cutting planes (b) Vertical cutting plane passing through the region experiencing maximum principal stress

The boulder's temperature and stress distributions will be illustrated on a series of cutting planes. Figure 2.7(a) illustrates the three equidistant horizontal cutting planes passing through a given boulder used to show the distribution of temperature and maximum principal stress within the boulder. The distribution of maximum principal stress will also be

Table 2.4: Radiation related parameters

Boulder's Diameter (m)	Threshold view factor	Number of pixels	Finite Element Model of Sun's Diameter (m)
0.150	10^{-12}	2000	0.100
0.200	10^{-12}	2000	0.100
0.250	10^{-12}	2000	0.100
0.300	10^{-12}	3000	0.150
0.500	10^{-12}	3000	0.400
0.625	10^{-12}	3000	0.200
0.750	10^{-12}	3000	0.150
0.875	10^{-12}	3000	0.292
1.000	10^{-12}	3000	0.250
1.250	10^{-12}	3000	0.500
1.500	10^{-12}	3000	0.500
2.000	10^{-12}	3000	0.400
3.000	10^{-12}	3000	0.750
5.000	10^{-12}	3000	1.250

depicted on a vertical cutting plane (Figure 2.7(b)). For any given boulder, the vertical cutting plane is perpendicular to the central horizontal cutting plane and will pass through the region experiencing maximum principal stress on that horizontal plane; this region is denoted by the yellow spot having an azimuth θ, measured from the north. The arrangement of sub-figures in Figure 2.8 is used consistently in this section to depict the temperature and maximum principal stress distribution for all boulders in this section.

Table 2.5: Thickness of element in the radial direction

Boulder's Diameter (m)	Layer 1 (m)	Layer 2(m)	Layer 3 (m)	Layer 4 (m)
0.150	0.00375	0.00375	0.005625	0.005625
0.200	0.005	0.005	0.0075	0.0075
0.250	0.00625	0.00625	0.009375	0.009375
0.300	0.0075	0.0075	0.01125	0.01125
0.500	0.003125	0.00625001	0.01875	0.01875
0.625	0.00390625	0.00390625	0.0234375	0.0234375
0.750	0.01875	0.01875	0.028125	0.028125
0.875	0.00546876	0.0109375	0.0328125	0.0328125
1.000	0.005	0.00833333	0.0375	0.0375
1.250	0.0078125	0.015625	0.046875	0.046875
1.500	0.009375	0.01875	0.05625	0.05625
2.000	0.01	0.0166667	0.075	0.075
3.000	0.00937498	0.0187501	0.1125	0.1125
5.000	0.0125	0.0208333	0.1875	0.1875

2.3.1 A 0.30 m diameter boulder

This sub-section presents the distribution of temperature and tensile stress in a boulder with 0.3 m diameter at 4:45 pm when the maximum principal stress reaches its peak magnitude at the surface. Figures 2.8(a) and (b) respectively illustrate the temperature distribution on the boulder surface, and on three horizontal cutting planes. The boulder's temperature at this time ranges from 9°C to 22°C and the warmest region lies on the SW face roughly facing the sun at this time, while the coolest point lies on the NE face of the boulder, in the shaded side.

The largest tensile stress at the surface is 1.8 MPa on the SW face near the hot-spot (Figures 2.8(c) and (d)). At this time the boulder's surface emits heat as the insolation decreases, while the interior warm domain persists directly under the SW face. This creates tension near the surface and compression in the interior. The maximum principal stress is slightly higher in the upper than the lower hemisphere.

The interior of the 0.30 m diameter boulder experiences the largest tensile stress of 1.3 MPa at 9:00 am, when it is warmest along its SE surface, reaching 13°C as it receives direct solar radiation, and coolest towards the NW side (Figures 2.9(a) and (b)). The surface tries to expand as it warms up while the relatively cooler interior resists, leading to tension in the interior and compression near the surface. The tension reaches a peak near the boulder's center. The distribution of tension is spherically symmetric, except that the domain of high tension is slightly elongated, and it is aligned with the NW-SE direction (at an angle of 135° from North; Figures 2.9(c) and (e)).

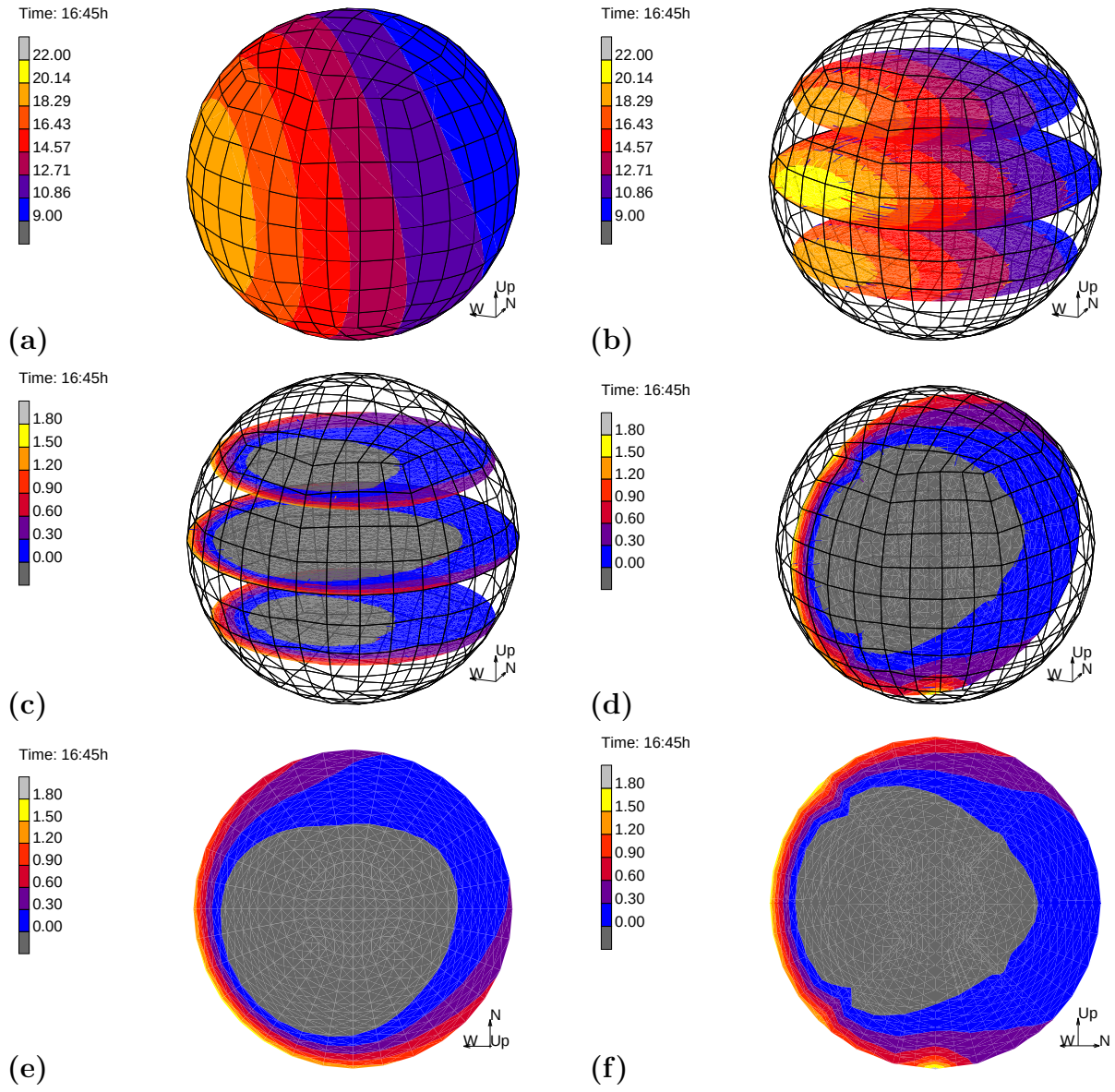

Figure 2.8: 0.30 m diameter boulder at 4:45 pm – time of peak tensile stress at the surface. Temperature distribution, in °C, (a) on the boulder surface (b) and along horizontal cutting planes. Perspective views of the maximal principal stress distribution, in MPa, (c) on horizontal cutting planes, and (d) a vertical plane passing through the location of maximal stress and striking NE-SW (at $\theta = 225°$ from north); 2d-view normal to the plane of maximum principal stresses (MPa) on the (e) central horizontal and (f) vertical cutting planes

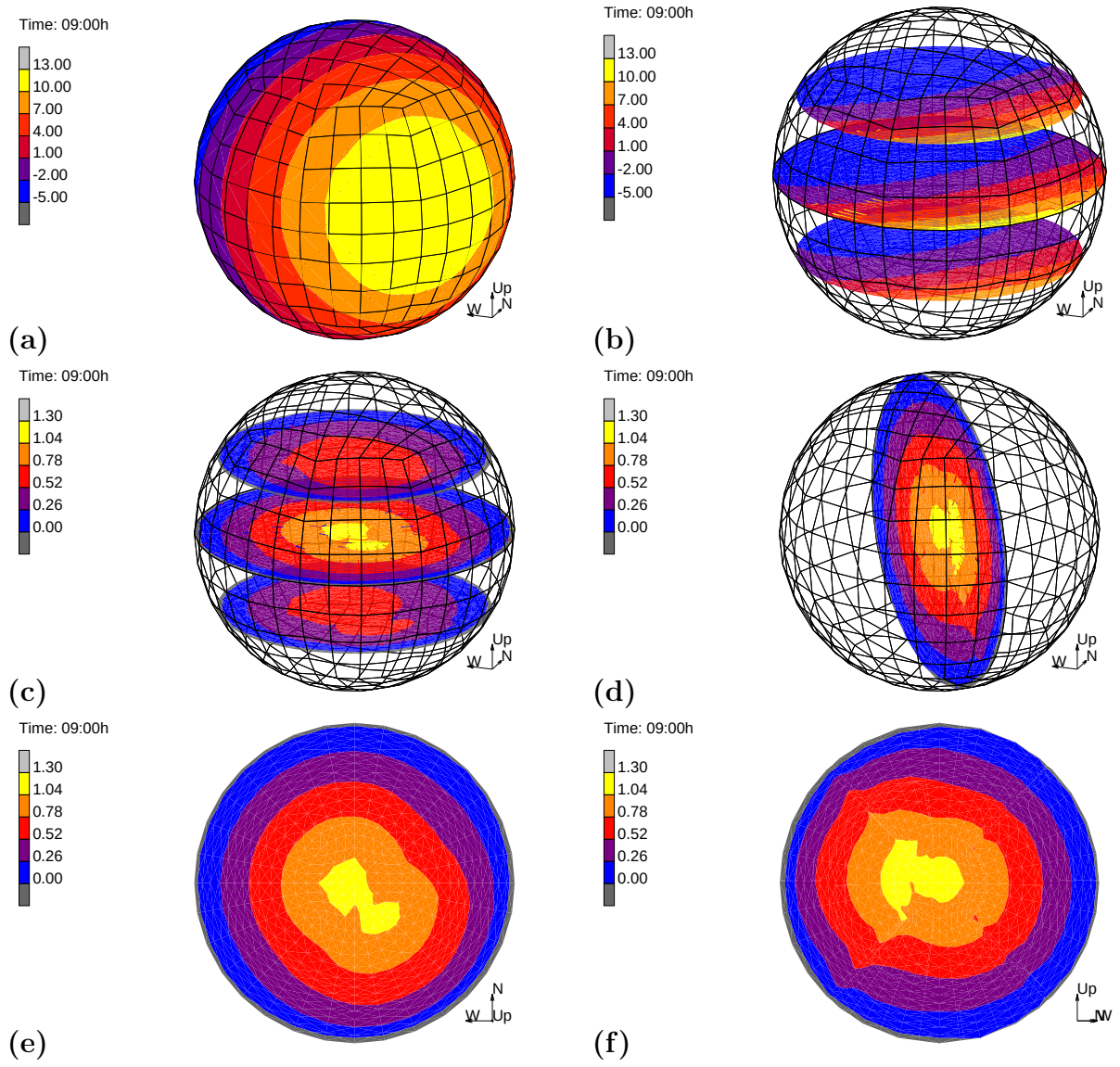

Figure 2.9: 0.30 m diameter boulder at 9:00 am – time of peak tensile stress at the interior. Temperature distribution, in °C, (a) on the boulder surface (b) and along horizontal cutting planes. Perspective views of the maximal principal stress distribution, in MPa, (c) on horizontal cutting planes, and (d) a vertical plane passing through the location of maximal stress and striking NE-SW (at $\theta = 135°$ from north); 2d-view normal to the plane of maximum principal stresses (MPa) on the (e) central horizontal and (f) vertical cutting planes

2.3.2 A 0.50 m diameter boulder

For a 0.50 m diameter boulder, tension peaks at the surface at 5:15 pm. Much as for a 0.30 m diameter boulder, there is a warm region near the SW face of the larger boulder while its side away from the sun remains cool (Figures 2.10(a) and (b)). The stress distribution is less spherically symmetric and the surface tension peaks at 2.0 MPa, about 30 minutes later than for smaller boulder. This peak occurs on the SW side of the boulder, at angle of 213.75° from north (Figure 2.10(e)) and inclined slightly (10-15) upward toward the sun (Figure 2.10(f)).

The interior of a 0.50 m diameter boulder takes longer to warm up than for a smaller boulder. The northern portion of the boulder is still cool at this time while the temperature of the boulder reaches its peak along the southern face (Figure 2.11(a) and (b)). The rise in temperature along the southern face causes the surface to expand, which pulls on the interior of the boulder, generating tension there. Similar to the 0.30 m diameter boulder, the domain of largest tensile stress is near the center of the boulder and slightly elongated toward the S-SW (200° from north; Figures 2.11(c) and (e)). The tensile stress in the interior reaches 2.1 MPa.

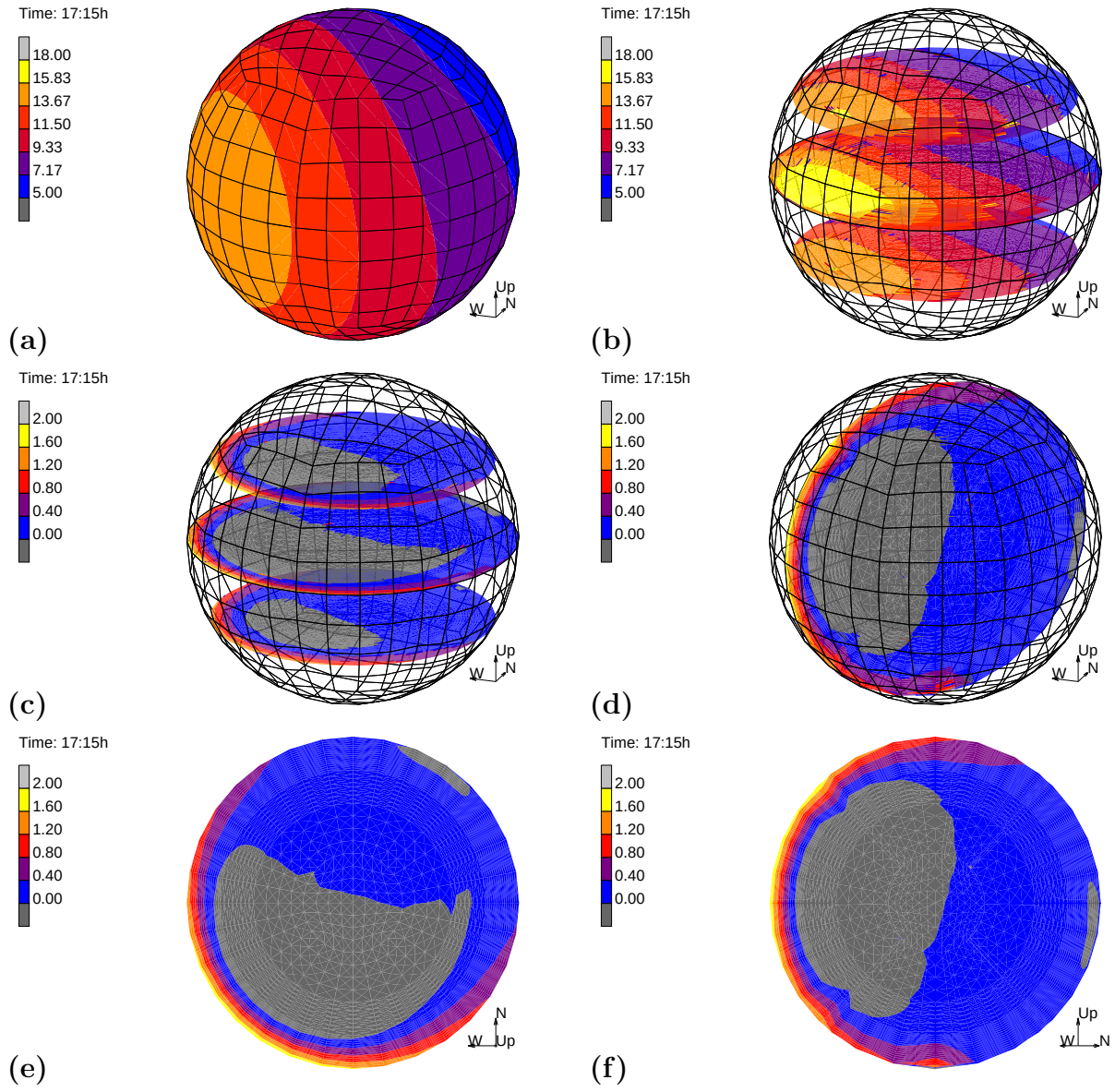

Figure 2.10: 0.50 m diameter boulder at 5:15 pm – time of peak tensile stress at the surface. Temperature distribution, in °C, (a) on the boulder surface (b) and along horizontal cutting planes. Perspective views of the maximal principal stress distribution, in MPa, (c) on horizontal cutting planes, and (d) a vertical plane passing through the location of maximal stress and striking NE-SW (at $\theta = 213.75°$ from north); 2d-view normal to the plane of maximum principal stresses (MPa) on the (e) central horizontal and (f) vertical cutting planes

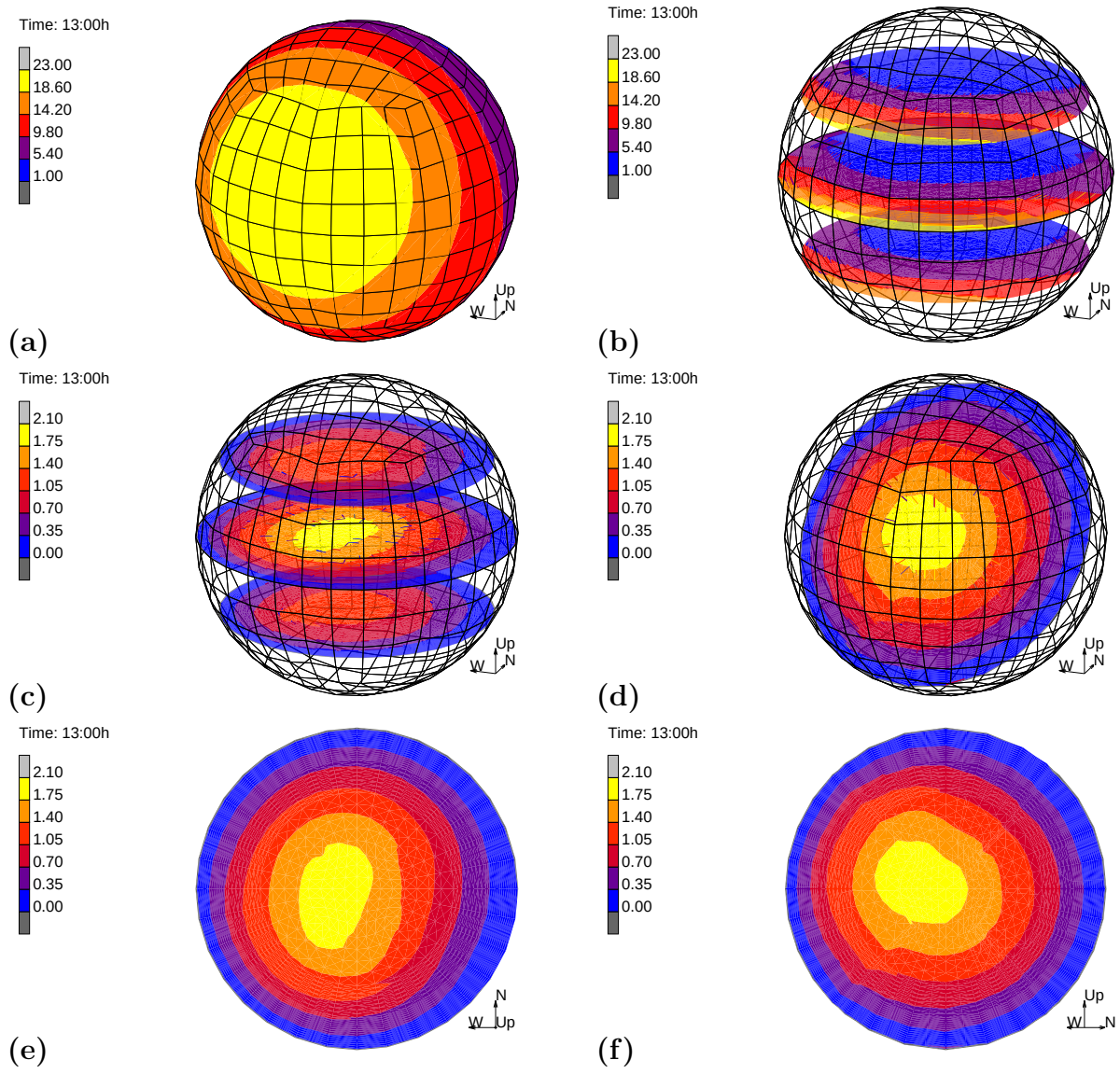

Figure 2.11: 0.50 m diameter boulder at 1:00 pm – time of peak tensile stress at the interior. Temperature distribution, in °C, (a) on the boulder surface (b) and along horizontal cutting planes. Perspective views of the maximal principal stress distribution, in MPa, (c) on horizontal cutting planes, and (d) a vertical plane passing through the location of maximal stress and striking NE-SW (at $\theta = 225°$ from north); 2d-view normal to the plane of maximum principal stresses (MPa) on the (e) central horizontal and (f) vertical cutting planes

2.3.3 A 1.00 m diameter boulder

A 1.00 m diameter boulder experiences largest tensile stress on the surface at 8:30 pm. The thermal mass of a boulder increases with its diameter, and a boulder with larger thermal mass takes longer to warm up and cool. At 8:30 pm, The SW interior of a 1.0 m diameter boulder remains warm while the surface emits heat. The NE portion which receives lesser insolation, remains relatively cooler and experiences minor variation in temperature (Figures 2.12(a) and (b)). At this time, a 0.30 m and a 0.50 m diameter boulders experience a relatively low variation in temperature throughout their bodies, which results in a lower magnitude of tensile stress at the surface compared to the 1.00 m diameter boulder. The highest magnitude of tensile stress at the surface is 2.7 MPa and is located between the center and SW face at an angle of 202.5° from the north (Figures 2.12(c) - (d)).

Tensile stress in the interior of a 1.0 m diameter boulder reaches its peak at 4:00 pm. A large NE portion of the boulder is relatively cooler and experiences very less variation in temperature at 4:00 pm, while the SW face of the boulder receives insolation and is warmer (Figures 2.13(a) and(b)). Compared to a 0.30 m and a 0.50 m diameter boulders, the peak of tensile stress is located relatively farther from the center (Figure 2.13(c) and (d)). Figures 2.13(e) and (f) denote that the domain of largest tensile stress is observed between center and SW face at an angle of 225° from north.

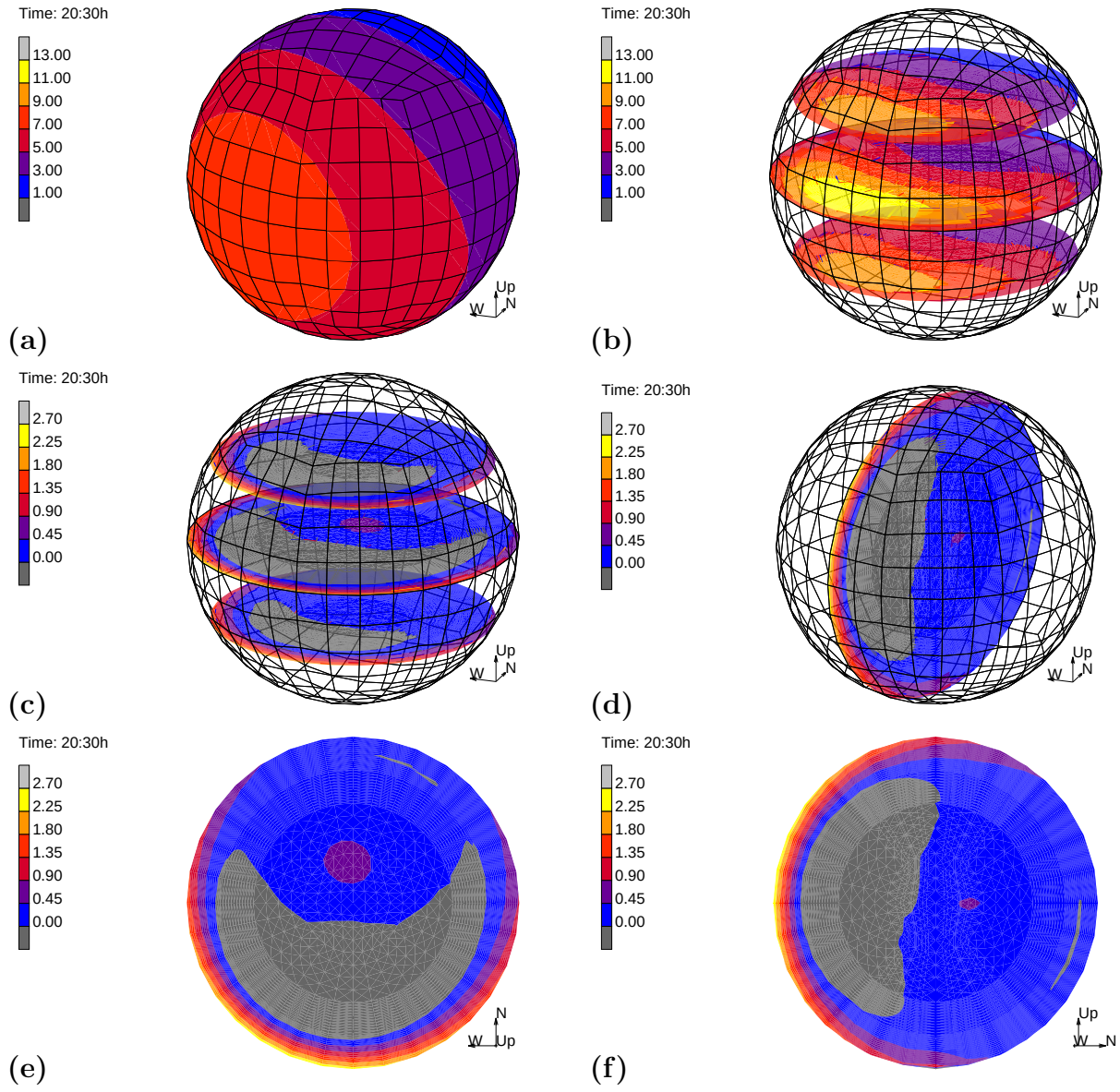

Figure 2.12: 1.00 m diameter boulder at 8:30 pm – time of peak tensile stress at the surface. Temperature distribution, in °C, (a) on the boulder surface (b) and along horizontal cutting planes. Perspective views of the maximal principal stress distribution, in MPa, (c) on horizontal cutting planes, and (d) a vertical plane passing through the location of maximal stress and striking NE-SW (at $\theta = 202.5°$ from north); 2d-view normal to the plane of maximum principal stresses (MPa) on the (e) central horizontal and (f) vertical cutting planes

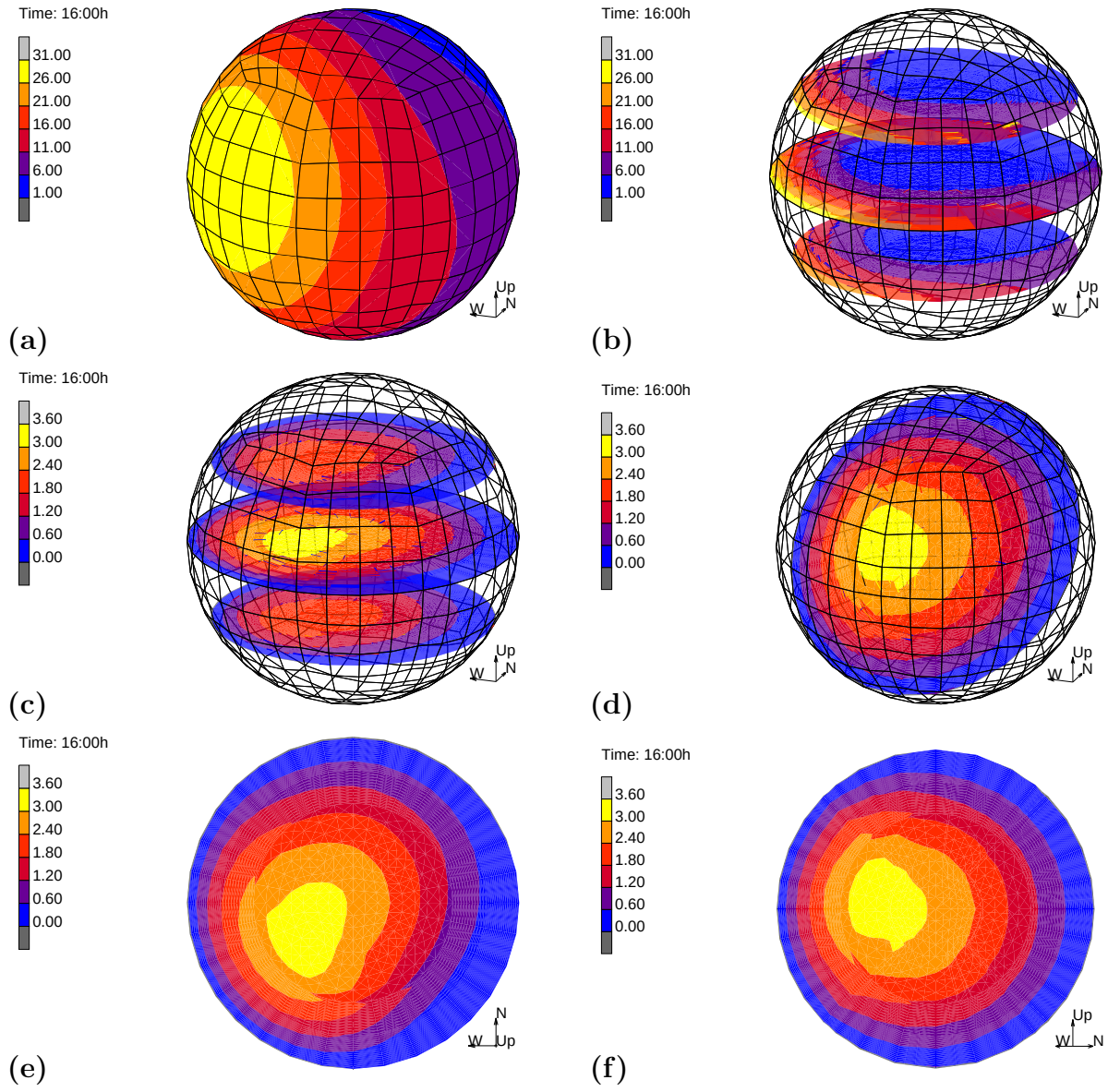

Figure 2.13: 1.00 m diameter boulder at 4:00 pm – time of peak tensile stress at the interior. Temperature distribution, in °C, (a) on the boulder surface (b) and along horizontal cutting planes. Perspective views of the maximal principal stress distribution, in MPa, (c) on horizontal cutting planes, and (d) a vertical plane passing through the location of maximal stress and striking NE-SW (at $\theta = 225°$ from north); 2d-view normal to the plane of maximum principal stresses (MPa) on the (e) central horizontal and (f) vertical cutting planes

2.3.4 A 3.00 m diameter boulder

A 3.00 m diameter boulder is able to retain the hot spot at the SW portion even after 13 hours past the sunset because of its larger thermal mass (Figures 2.14(a) and (b)). At 6:00 am, as the surface of the boulder loses heat to the atmosphere, it experiences a temperature between -5°C to 1°C. On the other hand, the SE interior is at relatively higher temperature between 10°C to 7°C. The boulder's surface tries to contract while cooling throughout the night, while the resistance from the warmer interior keeps on increasing and the tensile stress at the surface reaches its peak value of around 5.4 MPa at 6:00 am (Figure 2.14(c)). The largest tensile stress is located at an angle of 191.25°C from the north (Figure 2.14(d)). The tensile stress is confined within 0.13 m to 0.18 m from the surface and a large domain of the boulder is under compression (Figures 2.14(e) and (f)).

The tensile stress at the interior of a 3.00 m boulder reaches its peak at 4:15 pm. The exposure of the boulder to the sun from noon to afternoon hours raises the temperature at the surface to 30°C on the SW side while a major part of the interior remains relatively cool and shows little variation in temperature (Figures 2.15(a) and (b)). The temperature difference within 0.25 m from the surface on the SW face is around 18.6°, while the remaining portion of the boulder experiences a significantly low variation in temperature and remains relatively cool. This state of temperature pushes the tensile stress at the interior of the boulder to its peak. The largest tensile stress is located at an angle of 225° from north (Figure 2.15(d)) and has a magnitude of around 2.3 MPa. Unlike the boulders smaller than 3.00 m shown in this document, the domain of largest tensile stress in the 3.00 m diameter boulder is much closer to the surface than the center (Figures 2.15(e) and (f)).

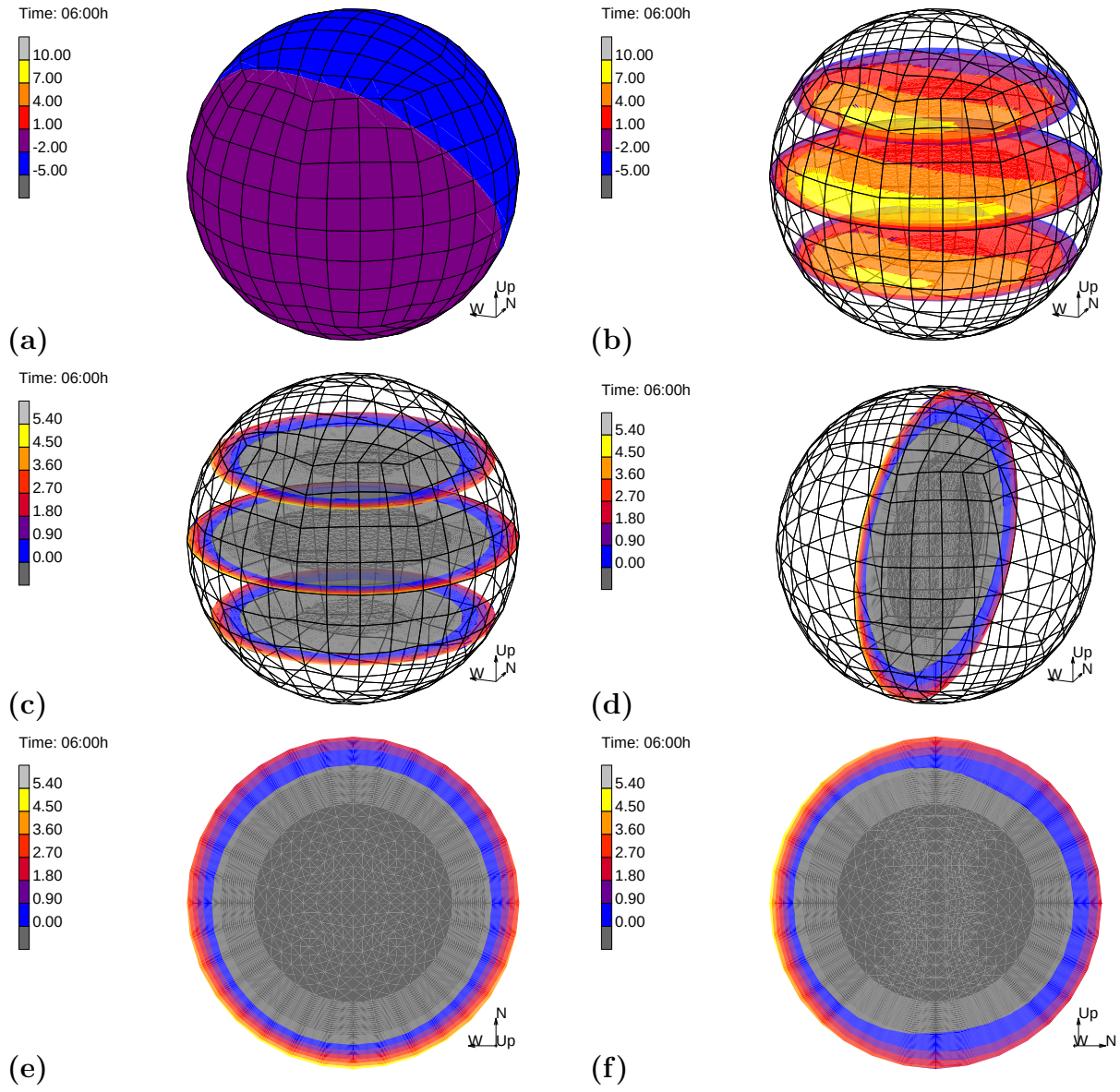

Figure 2.14: 3.00 m diameter boulder at 6:00 am – time of peak tensile stress at the surface. Temperature distribution, in °C, (a) on the boulder surface (b) and along horizontal cutting planes. Perspective views of the maximal principal stress distribution, in MPa, (c) on horizontal cutting planes, and (d) a vertical plane passing through the location of maximal stress and striking NE-SW (at $\theta = 191.25°$ from north); 2d-view normal to the plane of maximum principal stresses (MPa) on the (e) central horizontal and (f) vertical cutting planes

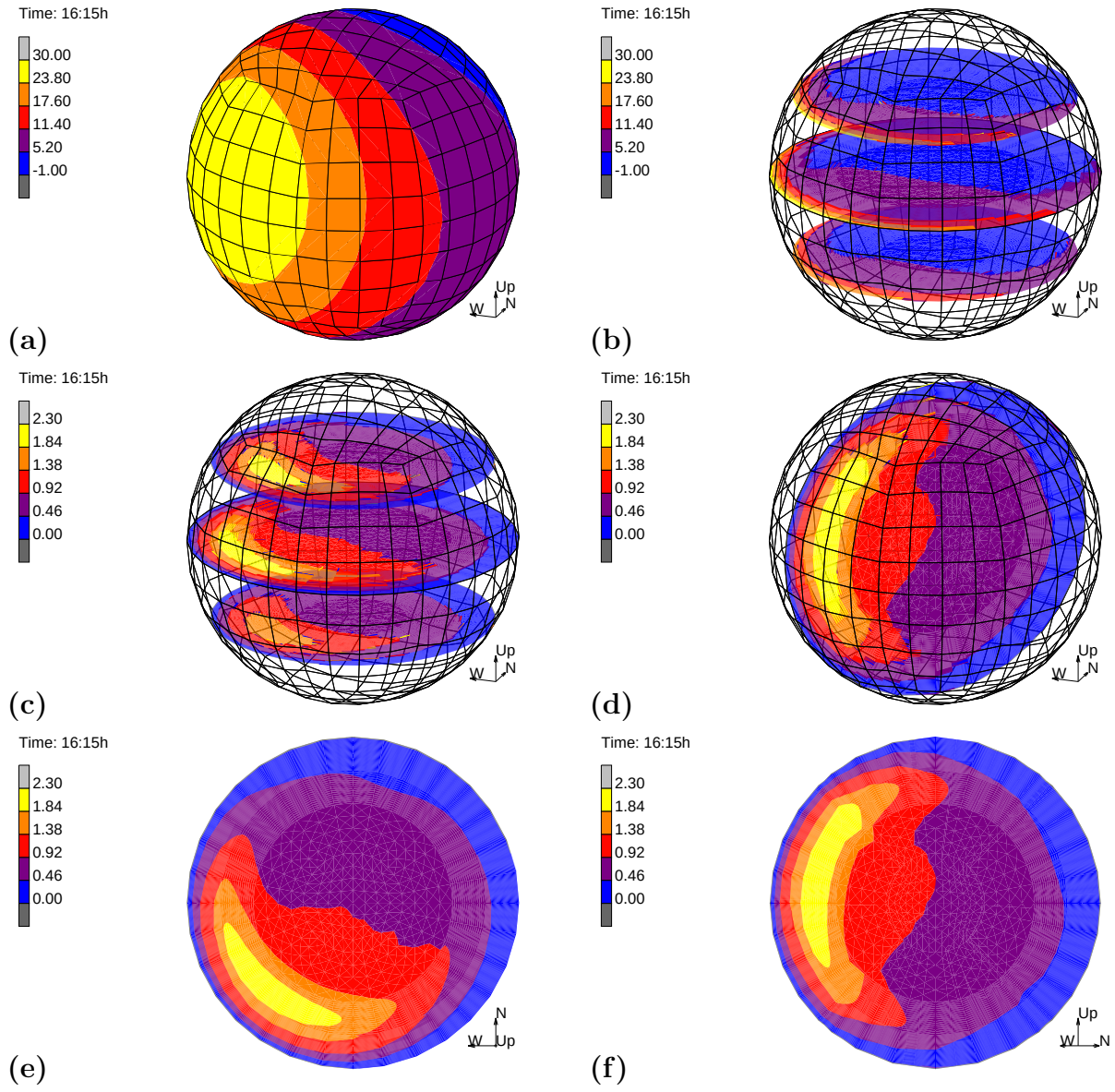

Figure 2.15: 3.00 m diameter boulder at 4:15 pm – time of peak tensile stress at the interior. Temperature distribution, in °C, (a) on the boulder surface (b) and along horizontal cutting planes. Perspective views of the maximal principal stress distribution, in MPa, (c) on horizontal cutting planes, and (d) a vertical plane passing through the location of maximal stress and striking NE-SW (at $\theta = 225°$ from north); 2d-view normal to the plane of maximum principal stresses (MPa) on the (e) central horizontal and (f) vertical cutting planes

2.3.5 A 5.00 m diameter boulder

The state of a 5.00 m diameter boulder at 6:30 am has been illustrated in Figure 2.16, and at this time the tensile stress on the surface reaches its peak magnitude of around 6.12 MPa. A large part of the boulder's southern interior is at relatively higher temperature between 11°C to 7.6°C, while the surface temperature is between -6°C to -2.6°C (Figures 2.16(a) and (b). The contracting surface experiences a large resistance from the interior due to which the tensile stress at the surface reaches its peak. The peak of tensile stress lies at an angle of 180° from the north (Figures 2.15(c)- (f)).

A 5.00 m diameter boulder experiences the peak of tensile stress at the interior at 10:15 am. As the boulder receives insolation after the sunrise, the surface begins to warm up, and the SE face reaches a temperature of 23° (Figures 2.16(a) and (b)). The interior of the boulder at this time is relatively cooler. This temperature distribution leads a 5.00 m diameter boulder to experience the peak of tensile stress at the interior. The peak occurs at a distance of 0.2 m from the surface, at an angle of 236.25° from north (Figures 2.16(c)-(f)), and has a magnitude of around 2.5 MPa.

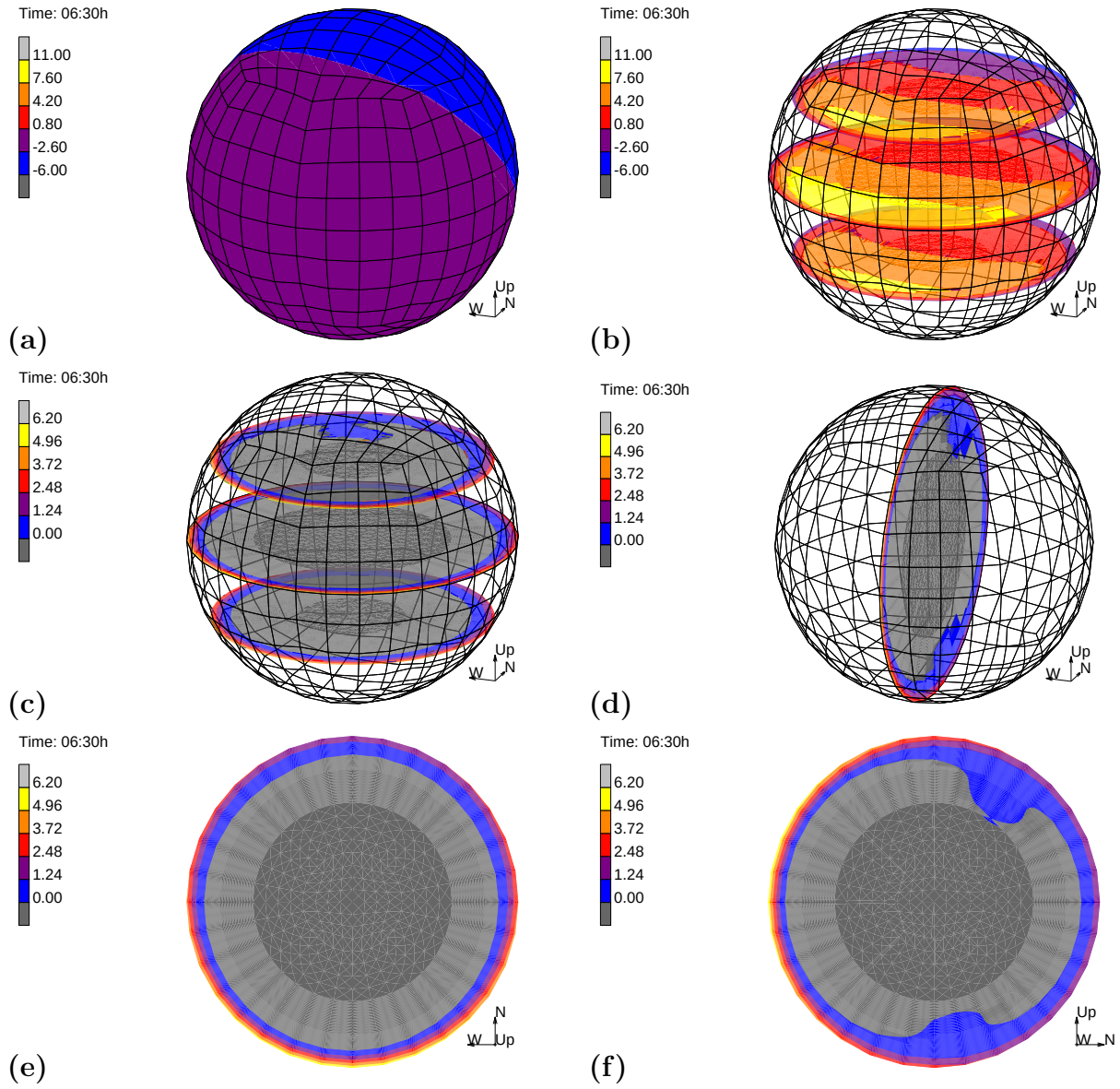

Figure 2.16: 5.00 m diameter boulder at 6:30 am – time of peak tensile stress at the surface. Temperature distribution, in °C, (a) on the boulder surface (b) and along horizontal cutting planes. Perspective views of the maximal principal stress distribution, in MPa, (c) on horizontal cutting planes, and (d) a vertical plane passing through the location of maximal stress and striking NE-SW (at $\theta = 180°$ from north); 2d-view normal to the plane of maximum principal stresses on (MPa) the (e) central horizontal and (f) vertical cutting planes

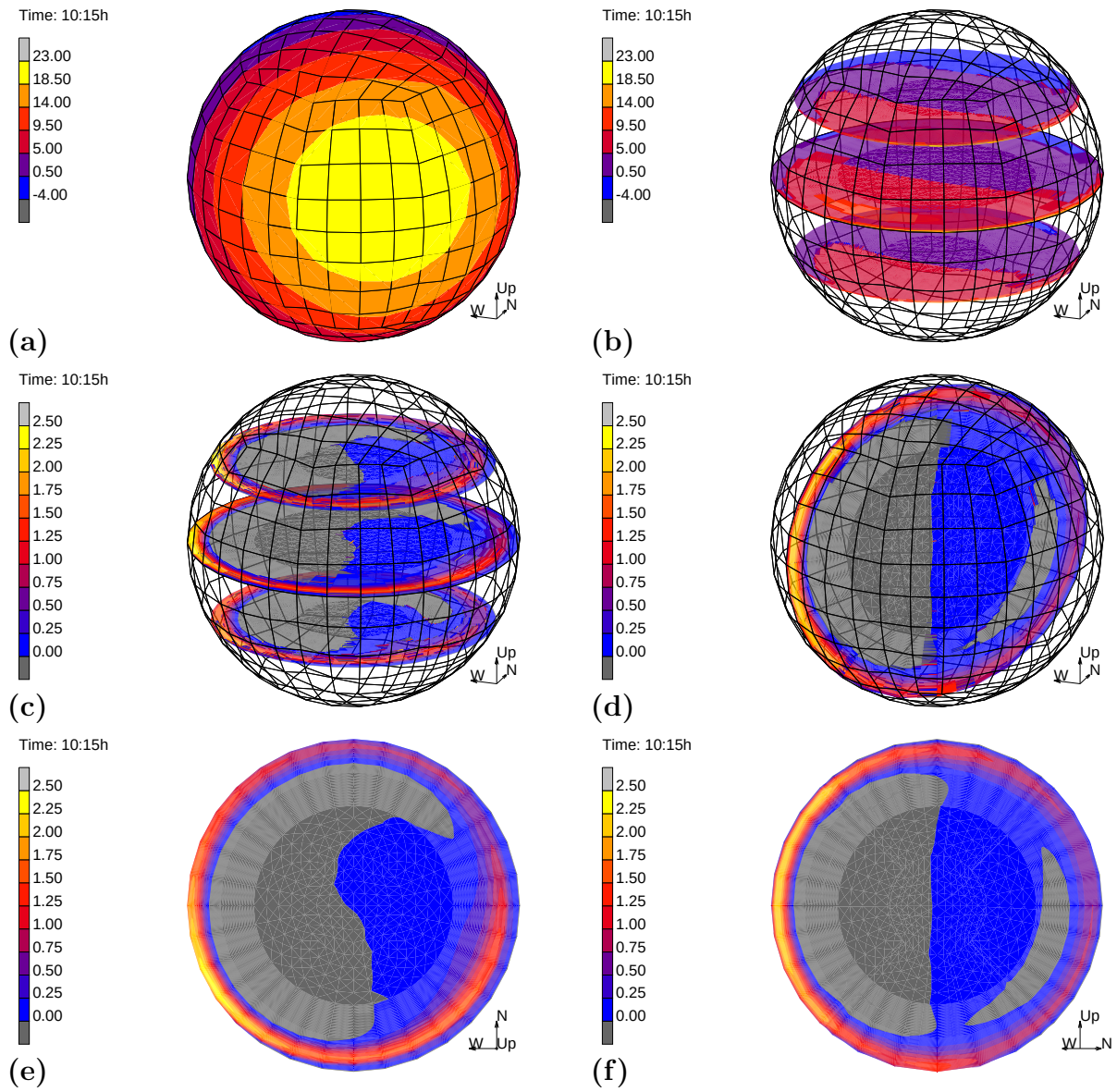

Figure 2.17: 5.00 m diameter boulder at 10:15 am – time of peak tensile stress at the interior. Temperature distribution, in °C, (a) on the boulder surface (b) and along horizontal cutting planes. Perspective views of the maximal principal stress distribution, in MPa, (c) on horizontal cutting planes, and (d) a vertical plane passing through the location of maximal stress and striking NE-SW (at $\theta = 236.25°$ from north); 2d-view normal to the plane of maximum principal stresses (MPa) on the (e) central horizontal and (f) vertical cutting planes

2.4 Location of significant tensile stresses in the interior of boulders

We now consider the stress state for the full range of boulder sizes analyzed when the maximum principal stress in the interior of each boulder reaches its peak. As discussed in the Section 2.3, the location of maximum principal stress varies significantly with boulder size (Figure 2.18). Unfortunately, this figure fails to show the variation in maximum principal stress inside the blue cloud which represents the lower limit of the maximum principal stress for each panel. The missing information can be seen through the figures illustrated in Section 2.3. The domain of significant tension increases in size with boulder size (Figure 2.18). The domain with elevated tensile stress within 25% of maximum principal stress is near the center of 0.30 and 0.50 m-diameter boulders, whereas it is closer to the SW side for 1.00 and 3.00 m-diameter boulders. For the 5.00 m diameter boulder, the region of high tension takes the form of a thick shell near the SW face.

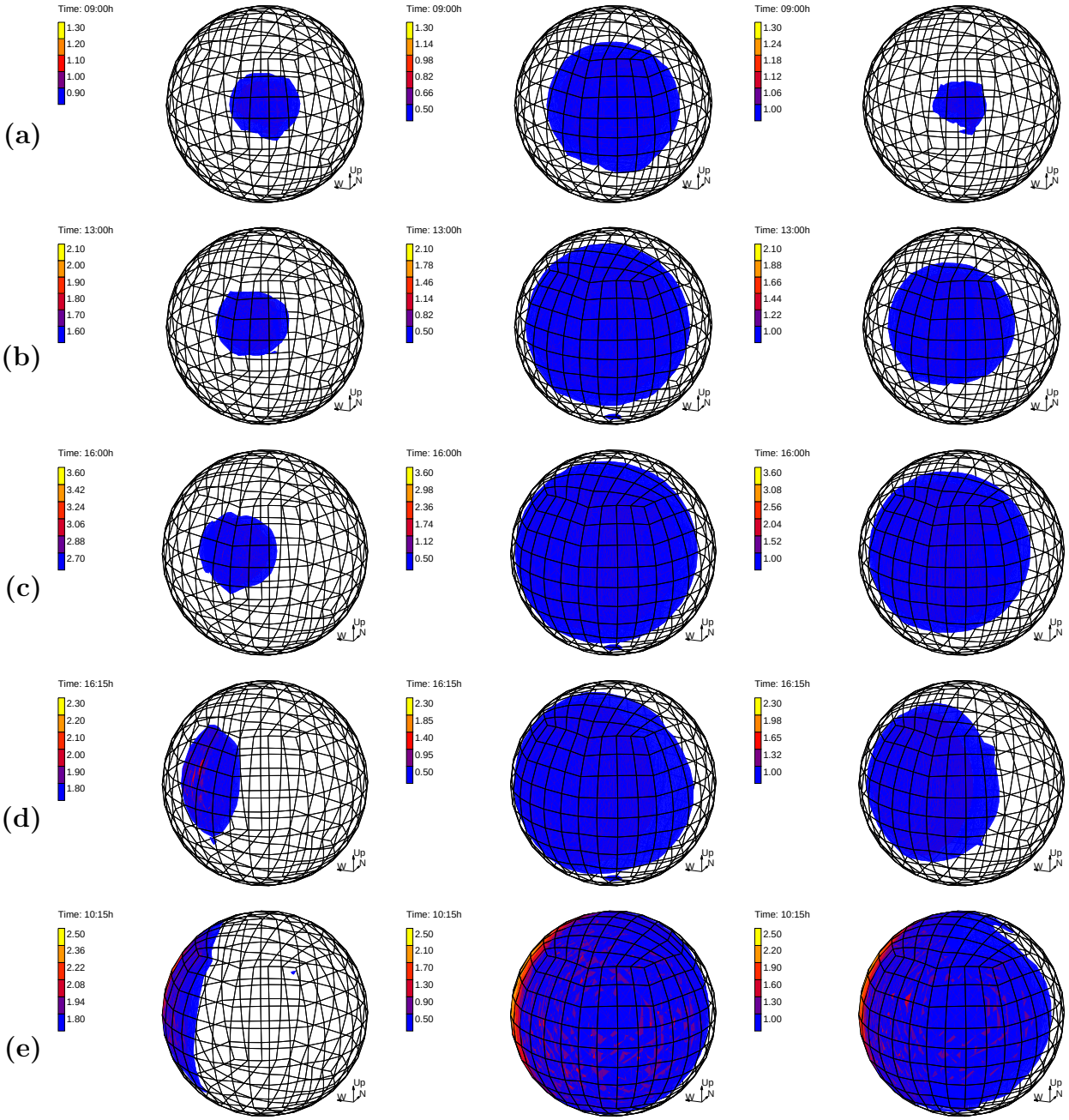

Figure 2.18: Domain experiencing significant interior tensile stress (MPa). Left column: top 25% maximum principal stress; Center column: tension ≥ 0.5 MPa; Right column: tension ≥ 1.0 MPa. (a) 0.30 m diameter, (b) 0.50 m diameter, (c) 1.00 m diameter, (d) 3.00 m diameter, (e) 5.00 m diameter

2.5 Maximum tensile stress over the course of a day

The maximum principal stress at each Gauss point within the boulder's finite element model over a period of one day at a time increment of fifteen minutes is illustrated in Figure 2.19.

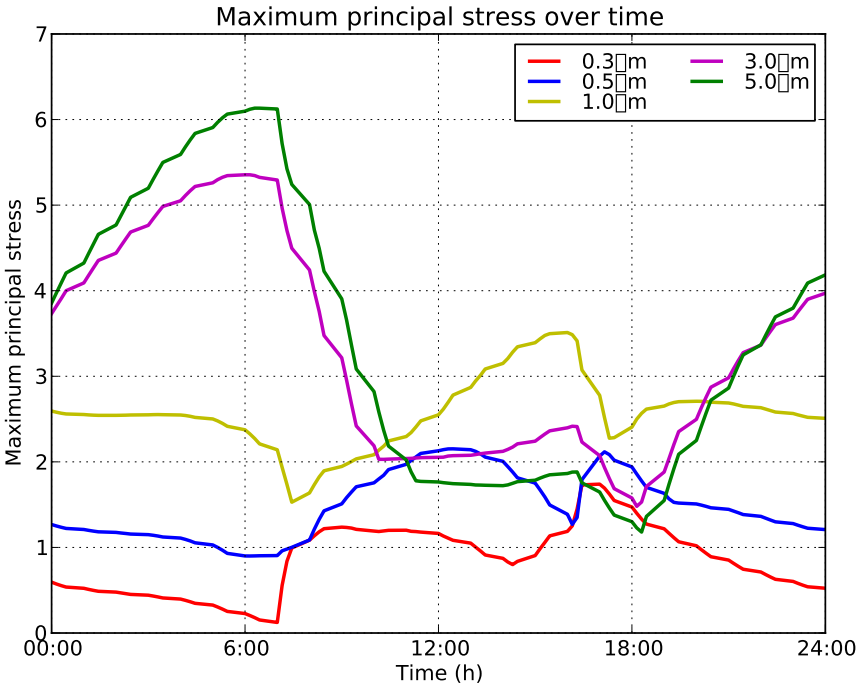

Figure 2.19: Maximum principal stress over time in boulders

The maximum principal stress in a 0.3 m diameter boulder decreases gradually till 7:00 am as its temperature is nearly uniform until sunrise when the stress increases sharply. The SE surface of the boulders warms quickly after the sunrise, while the NW part remains relatively cool. This temperature difference near the surface, leads to a sharp jump in the in maximum principal stress at the interior, as the boulder's surface expands and faces resistance from the interior. The maximum principal stress decrease progressively after 9:00 am till 3:00 pm. The surface starts cooling due to the decreasing insolation causing tension to develop at the surface, and reaches a peak value at 4:45 pm. Following this, the maximum principal stress decreases until sunrise as the boulder cools and the temperature difference in the boulder diminishes.

The maximum principal stress in a 0.50 m diameter boulder follows a similar trend to that of a 0.30 m diameter boulder, but the rise in maximum principal stress past the sunrise in a 0.50 m diameter boulder is relatively slow. The greater thermal mass of a 0.50 m diameter boulder also causes the maximum principal stress at the surface to rise relatively late. In a 1.00 m diameter boulder, the maximum principal stress declines slowly from midnight to 4:30 am following which it decreases rapidly till sunrise. As the boulder receives insolation and expands, the domain of dominant maximum principal stress shifts from surface to the interior, and the stress magnitude increases steadily till 4:00 pm after which it decreases till 5:00 pm. As the boulder loses heat past the sunset, the surface contracts and the dominant maximum principal stress shifts back to the surface and intensifies up to 8:00 pm. Subsequently, it starts declining slowly as the temperature within the boulder equilibrates over the night. Due to its considerable mass, the temperature within a 3.00 m diameter boulder changes relatively slowly and the interior remains at a significantly higher temperature than the surface before the sunrise, leading to an increase in the maximum principal stress at the surface through the night until the sunrise. At sunrise, the boulder starts receiving the insolation which warms the surface. Since the interior of the boulder is also warm at this point of time, the resistance to the expanding surface of the 3.00 m diameter boulder is low, hence the maximum principal stress decreases quickly. At 10:15 am, it starts increasing again as the tension in the boulder's interior increases. The maximum principal stress in the interior of the boulder reaches its peak value of 2.23 MPa at 4:15 pm. This is followed by decrease in the internal maximum principal stress as the boulder cools down after which the maximum principal stress at the surface starts rising at around 6:00 pm. The 5.00 m diameter boulder follows a similar trend to that of the 3.00 m boulder, but experiences a higher maximum principal stress at the surface because of larger resistive domain comprising the interior.

2.6 Effect of size on thermal stresses

Sections 2.3, 2.4, and 2.5 show that the magnitude of tensile stress, the size of the domain under tension and the timing of the thermal stress in boulders vary significantly with boulder diameter. In this section, we present the tensile stress at different locations within the boulders, that helps us better understand the numerical results.

The location inside a boulder is best characterized relative to the diurnal skin-depth, which follows from the analytical solution to a simplified thermal problem. We will explain the concept based upon a spherically symmetric problem, and present the underlying idea in what follows. The heat conduction equation for an axi-symmetric sphere with thermal diffusivity, κ, is given as

$$\frac{\partial T(t,r)}{\partial t} = \kappa \frac{1}{r^2} \frac{\partial}{\partial r} \left(r^2 \frac{\partial T(t,r)}{\partial r} \right) \ , \tag{2.1}$$

where t is time and r is radial distance from the center. For a periodic variation in surface temperature

$$T(t, r = R) = T_0 + \Delta T \sin(\omega t) \ , \tag{2.2}$$

where $\omega = 2\pi/P$ is the angular frequency for a period P, the skin depth follows as

$$\delta = \sqrt{\frac{2\kappa}{\omega}} = \sqrt{\frac{\kappa P}{\pi}} \ . \tag{2.3}$$

The closed form periodic solution for $T(t, r)$ can be expressed using this problem specific skin depth. (The actual solution has been omitted.) The sub-surface peak of maximum principal stress in the finite element models of the boulders of different diameters was roughly observed to be at around $\sqrt{\kappa P}$, which was approximately equal to 1.77 skin depth. Figure 2.20 illustrates the peak of maximum principal stress at the surface during morning hours, at 1.77 skin depth ($\sqrt{\kappa P}$) below the surface, and at the center of the boulder.

Figure 2.20 illustrates a section of numerical results, the peak of maximum principal stress at the surface during morning hours, at 1.77 skin depths, and at the center of the boulder. The peak of maximum principal stress at the surface during morning hours increases with radius up to 5.00 m where it approaches a limiting value of 6.2 MPa. The maximum principal stress at the boulder's center and at 1.77 skin depth increase till the boulder reaches a diameter of 1.00 m after which they start decreasing. These results are in agreement

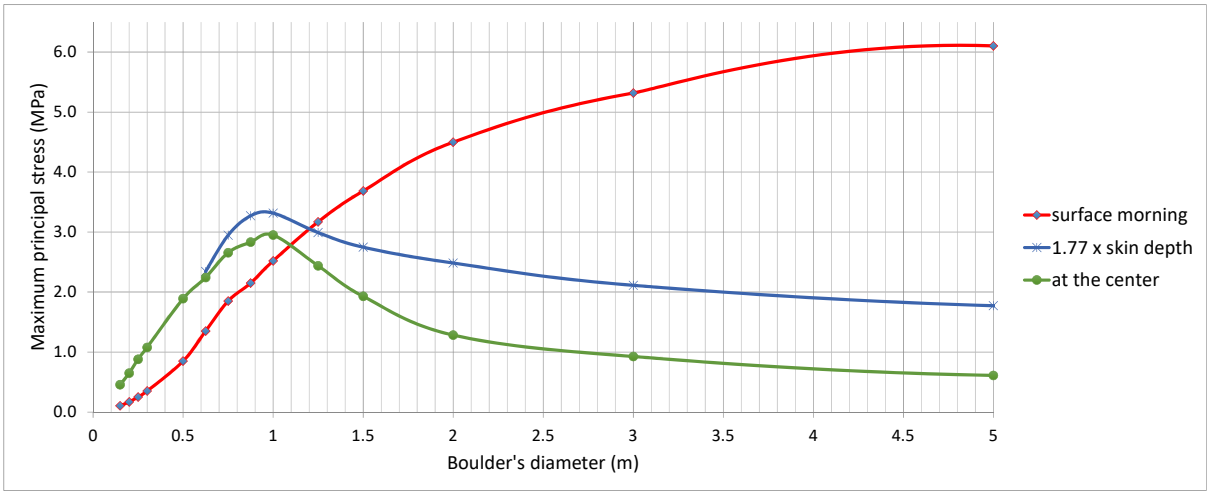

Figure 2.20: Effect of boulder size on maximum principal stress

with and complement Figure 2.19, which shows that the maximum principal stress at the surface increase with boulder's diameter, while maximum principal stress at the interior starts decreasing after the boulder's diameter exceeds 1 m. The boulders with diameter lesser than 0.625 m have radius lesser than 1.77 skin depth and hence the blue curve corresponding to them is absent in the Figure 2.20. It can also be observed that the maximum principal stress at 1.77 skin depth is higher then at the center of the boulders.

2.7 Summary and conclusions

This chapter sheds light on how the temperature and maximum principal stress in spherical boulders of various sizes vary through a day.

The peak of maximum principal stress at the boulder's surface increases with boulder's diameter and reaches a limiting value of around 6.2 MPa at a diameter of 5.00 m. In contrast, the peak of maximum principal stress in the boulder's interior increases up to a diameter of 1 m and decreased for larger.

The domain of elevated tensile stress within boulders depends sensitively on boulder size. At the time when the principal stress is largest in the interior, the most highly stressed domain is close to the core of boulders smaller than 0.5 m in diameter, whereas it is closer to the boulder surface for larger boulders. The volume of this stressed domain relative to that of the boulders, on the other hand, remained relatively constant. Since fracture in brittle materials initiates from the pre-existing flaws, the size of the domain of high stress plays a significant role in determining its strength. The probability of crack growth in boulders that experience different maximum principal stress, in terms of magnitude, location, and extent, is addressed in the next chapter.

Chapter 3

PROBABILITY OF CRACK GROWTH

3.1 Introduction

Our 3d coupled thermo-mechanical finite element simulations showed us that the spatial distribution of principal tensile stresses varied significantly with boulders size. In this chapter, we will assess the probability of sub-critical crack growth and its location in boulders of different sizes based on the time varying stressed domain size and magnitude of tensile principal stress, using the Weibull Theory. This study is a step towards determining the relationship between the size of a boulder, size of tensile stress domain and magnitude of stress as developed in Chapter 2, and probability of crack growth in this chapter.

Leonardo da Vinci measured the strength of iron wires and found that the strength varied inversely with wire length. This observation lead him to conclude that a material's strength is controlled by its flaws, since a longer wire corresponded to a larger sample volume, the probability of sampling a region containing a flaw increased (Anderson 2012). This was one of the first recorded studies that provided clues about the root of fracture. Centuries later, the first quantitative analysis about the role of flaws in fracture was provided by Inglis 1913. He analyzed a flat plate with an elliptical hole, which was subjected to tensile stress, σ (Figure 3.1). He assumed that the dimensions of the plate was much larger than the hole and that the plate boundaries did not have any effect on the hole. Inglis found that the stress at the crack tip, A, was amplified to

$$\sigma_A = \sigma(1 + 2\sqrt{\frac{a}{\rho}}) \ , \tag{3.1}$$

where σ_A is the value of amplified stress at point A, a is length of the semi-major axis, b is the length of the semi-minor axis, and ρ is the radius of curvature at A, which is given by

$$\rho = \frac{b^2}{a} \ . \tag{3.2}$$

Inglis proposed that pre-existing flaws in the materials amplified the applied stresses near

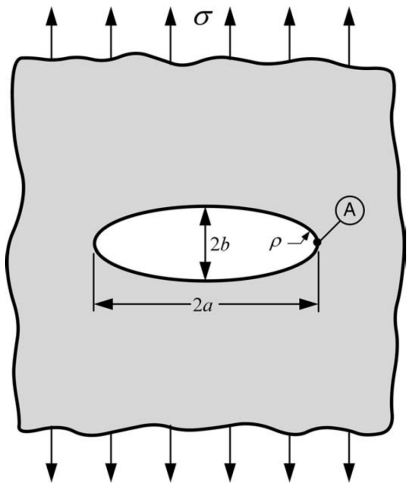

Figure 3.1: A through-thickness elliptical hole in an infinitely wide plate subjected to a remote tensile stress(Anderson 2012)

the flaw which caused the atomic bonds to rupture and lead to crack propagation. The ratio, σ_A/σ was referred as stress concentration. This theory, however, faced a mathematical difficulty as it predicts infinite stress at the tip of a sharp crack whose radius of curvature is zero, which implies that a material containing a sharp crack would fail upon application of an infinitesimal load.

The limitations of Inglis's theory lead Griffith (1893-1963) to develop a fundamental approach for predicting fractures in brittle materials caused by the pre-existing flaws. Griffith 1920 proposed that crack-propagation occurs when an incremental increase in a crack's length does not change the net energy of the system.

The net energy of a flat plate with a crack of length $2a$, thickness B, and subjected to tensile stress σ (Figure 3.2), is given by $U + S$, where U denotes the strain energy released in the creation of a through-thickness crack, and S is the increase in the surface energy due to the new surfaces formed by the crack. Assuming that the crack is much smaller than the plate, and the crack is unaffected by the plate boundaries, Griffith, using the solution derived by Inglis 1913 expressed the strain energy U, released in the creation of a through-going crack of length $2a$ as

$$U = -\frac{\pi\sigma^2 a^2 B}{E} \ , \tag{3.3}$$

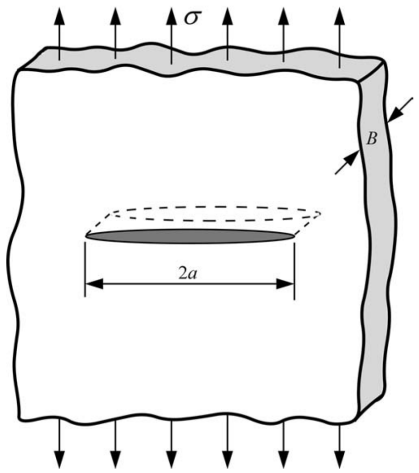

Figure 3.2: A through-thickness crack in an infinitely wide plate subjected to a remote tensile stress(Anderson 2012)

where E represents the modulus of elasticity of the plate. The gained surface energy S, is given as

$$S = 4a\gamma_s B \ , \tag{3.4}$$

where γ_s is the energy per unit area needed to create a new free surface. The factor 4 in Equation 3.4 arises because of there being two crack surfaces of length $2a$. According to Griffith, crack propagation will occur in the flat plate, if

$$-\frac{\partial U}{\partial a} = \frac{\partial S}{\partial a} \ . \tag{3.5}$$

Substituting Equations 3.3 and 3.4 in Equation 3.5 yields

$$\frac{2\pi\sigma^2 a}{E} = 4\gamma_s \ . \tag{3.6}$$

Solving Equation 3.6 for σ gives the fracture strength, σ_f, as

$$\sigma_f = \sqrt{\frac{2E\gamma_s}{\pi a}} \ . \tag{3.7}$$

Griffith obtained a good agreement between Equation 3.7 and experimental fracture strength of glass, however his theory was limited to brittle materials (Anderson 2012). Irwin 1948

and Orowan 1949 independently extended the application of Griffith's research to ductile materials. They proposed that the fracture strength of a material is equal to

$$\sigma_f = \sqrt{\frac{2E\left(\gamma_s + \gamma_p\right)}{\pi a}} \ . \tag{3.8}$$

where γ_p refers to the plastic work per unit area of surface created and is typically much larger than γ_s (Anderson 2012). The term $\gamma_s + \gamma_p$ is called fracture energy, w_f.

Irwin 1956 defined $\partial U/\partial a$ as strain energy release rate G_c, which, for a given material, can be found experimentally. Anderson 2012 stated the condition for sub-critical (stable) crack growth as

$$G_c = 2w_f \tag{3.9}$$

and

$$\frac{\partial G_c}{\partial a} \leq \frac{\partial\left(2w_f\right)}{\partial a} \ , \tag{3.10}$$

and unstable crack growth as

$$\frac{\partial G_c}{\partial a} \geq \frac{\partial\left(2w_f\right)}{\partial a} \ . \tag{3.11}$$

These studies have provided the foundation for our understanding of the role of material flaws in crack growth. Fracture in rocks is generally brittle, taking place with little or no preceding plastic deformation. The direction of crack propagation is nearly perpendicular to the direction of tensile stress. The stress concentration in the brittle materials near the tip of pre-existing flaws lead to crack propagation in either transgranular or intergranular manner. Transgranular fractures are characterized by splitting of crystals, or grains, along specific crystallographic planes, irrespective of grain boundaries. Intergranular fracture on the other hand involves crack propagation along grain boundaries, which is common in materials with grain boundaries that are weaker than grains (Anderson 2012).

The variation in strength of identical brittle specimens can be attributed to differences in the arrangement of grains or crystals at microscopic level. According to Anderson 2012:

> "Two nominally identical specimens made from the same material may display vastly different toughness values because the location of the critical fracture-triggering particle is random. If one specimen samples a large fracture-triggering particle near the crack tip, while the fracture trigger in the other specimen is

> further from the crack tip, the latter specimen will display a higher fracture toughness, because a higher load is required to elevate the stress at the particle to a critical value."

Additionally, among the two brittle specimens made up of same material, but, with different cross sections, a higher probability of failure can be expected in the specimen with larger cross section, since it will have a larger number of pre-existing flaws. A clear understanding of this phenomenon plays a crucial role when assessing the probability of crack growth in boulders of different sizes. Since high tensile stresses can occur over a small volume in one boulder while lower tensile stresses can occur over a larger volume in another boulder, studying the magnitude of peak stress alone is not be sufficient.

Such variation of strength in specimens due to differences in the arrangements of flaws, grains or crystals, and overall volume have been addressed by Weibull 1939 and subsequent researchers (e.g.; Weibull 1939; Anderson and Stienstra 1989; Lin et al. 1986; Jayatikala and Trustrum 1977; Petrovic 1987; Danzer et al. 2008). Using the fundamental laws of probability, Weibull 1939 proposed an approach useful to study the inconsistency in strength of ideal brittle specimens.

3.2 Weibull theory

Weibull 1951 proposed a Cumulative Density Function (CDF) to find probability of an item having value lesser than σ as

$$F(\sigma) = 1 - \exp\left[-\left(\frac{\sigma - \epsilon}{\sigma_o}\right)^m\right] , \tag{3.12}$$

where ϵ is the lower limit of σ, σ_o is a scale parameter, and m is a shape parameter. The corresponding probability density function (PDF) is given by

$$f(\sigma) = \frac{\partial F(\sigma)}{\partial \sigma} = \frac{m}{\sigma_o}\left(\frac{\sigma - \epsilon}{\sigma_o}\right)^{m-1} \exp\left[-\left(\frac{\sigma - \epsilon}{\sigma_o}\right)^m\right] , \quad \sigma \geq \epsilon . \tag{3.13}$$

Figure 3.3 illustrates the Weibull's PDF and CDF for different values of m when $\sigma_o = 1.0$ and $\epsilon = 0.0$. Small values of m result in a relatively wider spread of PDF. Weibull's CDF for $\epsilon = 0$, commonly known as two-parameter Weibull distribution, has been widely used for modeling the lifetime of products and components (Jiang and Murthy 2011).

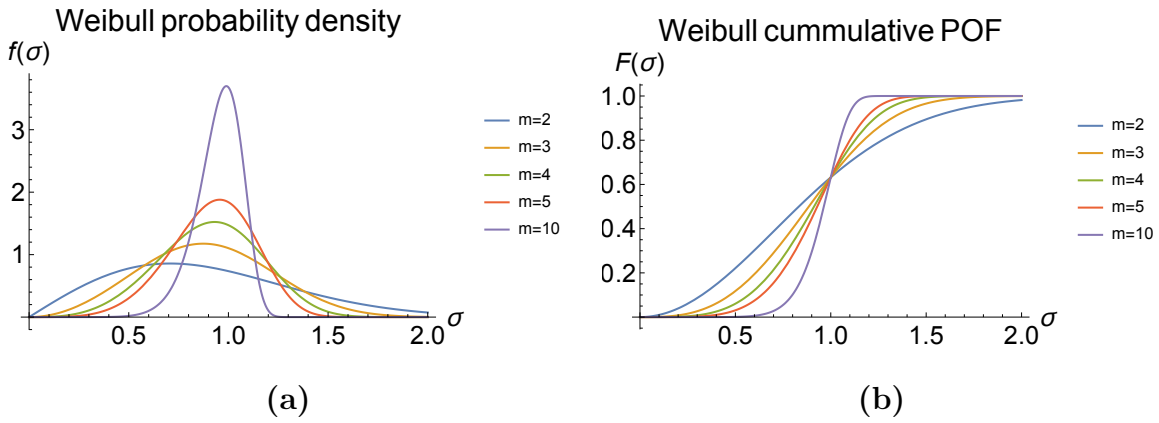

Figure 3.3: (a) Probability density function $f(\sigma)$ (b) Cumulative density function $F(\sigma)$

Weibull 1939 proposed the following relation for the probability of rupture $F(\sigma)$, of a material of volume V, subjected to tensile stress σ:

$$F(\sigma) = 1 - \exp(-B) \ , \tag{3.14}$$

where B is referred to as risk of rupture and is given as

$$B = \int_V n(\sigma)\, dV \ , \tag{3.15}$$

with the stress function

$$n(\sigma) = \left(\frac{\sigma}{\sigma_o}\right)^m \ , \tag{3.16}$$

For an isotropic brittle material, the function $n(\sigma)$ is independent of position and volume dV, and the orientation of tensile stress. Equation 3.14 is a two parameter Weibull function which incorporates the size of a specimen through its volume, V.

Parameter identification can be performed from experiments as follows. The mean value of $f(\sigma)$ according to Equation 3.13 is obtained as

$$\mu_\sigma = \sigma_o \Gamma\left(1 + \frac{1}{m}\right) \tag{3.17}$$

and the coefficient of variation as

$$C_{v\sigma} = \left[\frac{\Gamma\left(1+\frac{2}{m}\right)}{\Gamma^2\left(1+\frac{1}{m}\right)} - 1\right]^{1/2} \ , \tag{3.18}$$

where $\Gamma()$ represents the gamma function. At the same time, the mean μ_σ, and coefficient of variation $C_{v\sigma}$, can be obtained from experimental data. Equations 3.17 and 3.18 then can be solved for Weibull parameters, m and σ_o.

For a material subjected to three dimensional (3d) state of stress, Weibull 1939 stated that the risk of rupture can be calculated by computing the effect as the compound probability of all possible fracture planes. This is achieved through integration over all possible orientations defined through unit normal vectors. This set of unit vectors represents a unit sphere, S, of which only one half describes unique orientations (3.4). This leads to 3d version of risk of rupture per unit volume as

$$B = \frac{2m+1}{2\pi} \int_0^{\pi/2} \int_{-\pi}^{\pi} n(\sigma_1, \sigma_2, \sigma_3)\, \cos(\psi)\, d\varphi\, d\psi \ , \tag{3.19}$$

where the stress function $n(\sigma_1, \sigma_2, \sigma_3)$ is given by

$$n(\sigma_1, \sigma_2, \sigma_3) = \left(\frac{\sigma_1 \cos^2(\psi)\cos^2(\varphi) + \sigma_2 \sin^2(\psi)\cos^2(\varphi) + \sigma_3 \sin^2(\varphi)}{\sigma_o} \right)^m \ . \tag{3.20}$$

σ_1, σ_2, and σ_3 in Equation 3.20 represent the principal stresses. Considering the computa-

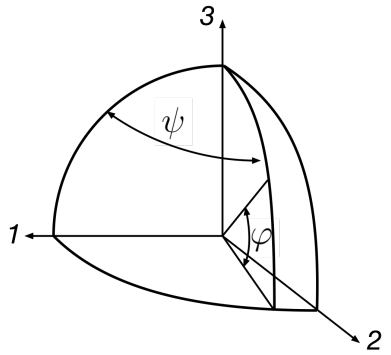

Figure 3.4: Reference angles used by Weibull 1939 to compute risk of rupture for 3d state of stress

tionally intensive nature of Equation 3.19, Mackenzie-Helnwein 2017 proposed a simplified tensor function for the risk of rupture of a material of volume, V, subjected to three dimensional state of stress as

$$B = \int_V n(\sigma_1, \sigma_2, \sigma_3)\, \frac{dV}{V_o} \ , \tag{3.21}$$

where V_o represent the reference volume for which Weibull parameters were identified. The proposed stress function $n(\sigma_1, \sigma_2, \sigma_3)$, for the corresponding B is

$$n(\sigma_1, \sigma_2, \sigma_3) = \left(\frac{\sigma_1}{\sigma_o}\right)^m + \left(\frac{\sigma_2}{\sigma_o}\right)^m + \left(\frac{\sigma_3}{\sigma_o}\right)^m + 3\left(\frac{\sigma_1\sigma_2\sigma_3}{\sigma_o}\right)^{m/3} . \tag{3.22}$$

It was assumed that crack growth in brittle materials are influenced only by tensile stress, and hence, σ_1, σ_2, and σ_3 in Equation 3.22 was considered zero if compressive.

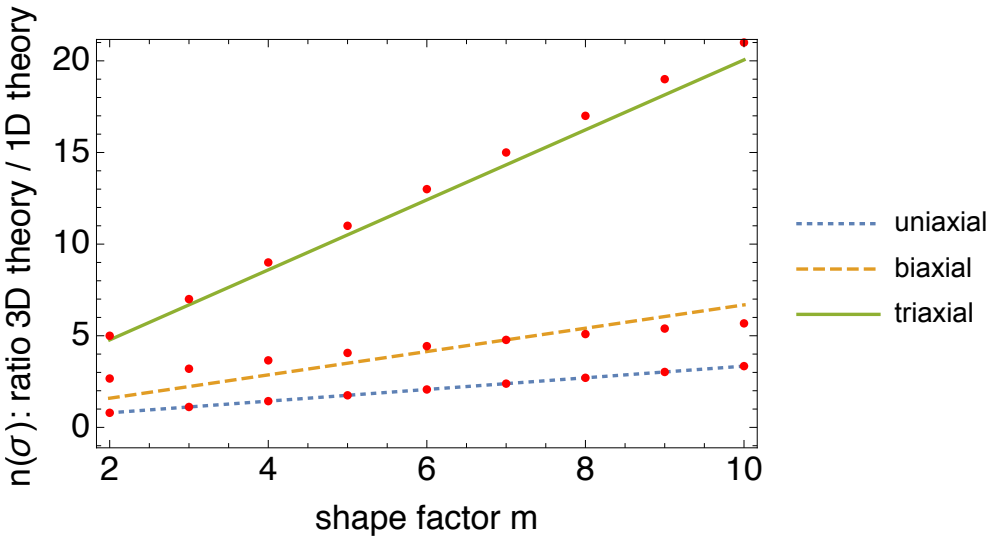

Figure 3.5: Risk of Rupture using the surface integral by Weibull 1939 (red dots) versus the simplified form by Mackenzie-Helnwein 2017 (solid lines)

Figure 3.5 illustrates the risk of rupture computed using Weibull 1939 and Mackenzie-Helnwein 2017 for uniaxial, biaxial ($\sigma_1 = \sigma_2$) and triaxial ($\sigma_1 = \sigma_2 = \sigma_3$) state of stress. respectively. It can be seen that Equation 3.21 proposed by Mackenzie-Helnwein 2017 is in reasonably good agreement with Equation 3.19 by Weibull 1939.

3.3 Adaption of Weibull theory to evaluate Probability of an Event (POE), leading to crack growth

We have carried out a probabilistic study of the effects of the time varying magnitude, location and spatial extent of solar induced stresses on sub-critical crack growth in boulders. Our study is based on Weibull theory, however, instead of trying to find the probability of

rupture as in Weibull 1939, we are applying it more generally to evaluate the probability of an event (POE). The term "event" stands for any crack related activity, including initiation, propagation, damage evolution, etc., detectable through acoustic emission measurements. The risk of rupture, B, mentioned in Section 3.2 now refers to the 'risk of event' for this research and has been calculated using Equation 3.21 proposed by Mackenzie-Helnwein 2017 to reduce the computational demand. σ_o, V_o and m to compute the risk of event using Equation 3.21 were taken as 1 MPa, 1 m^3, and 15, respectively. The value of m was chosen following a suggestion by Nakamura et al. 2007 for granite specimens.

3.4 Methodology to compute POE within a boulder

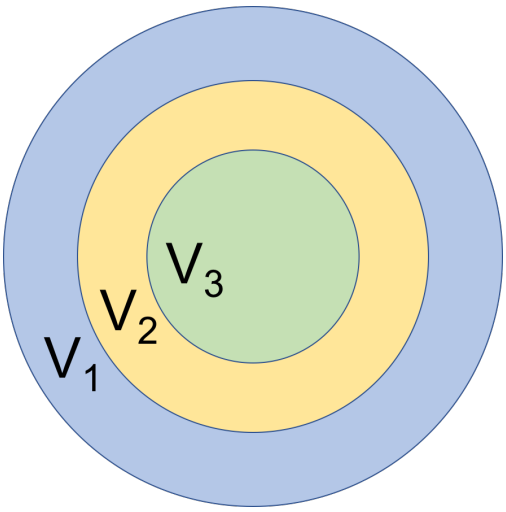

Figure 3.6: Sphere made up of different layers

Figure 3.6 illustrates a sphere of volume V, which for example is made up for three layers. The volume of constituent layers of the sphere have been referred as V_1, V_2, and V_3. For the given sphere

$$\int_V F\, dV = \sum_{i=1}^{3} \int_{V_i} F\, dV \ , \tag{3.23}$$

where F denotes an arbitrary function.

Substituting F in Equation 3.23 with the stress function $n(\sigma_1, \sigma_2, \sigma_3)$, from Equation 3.22

yields

$$B = \int_V n(\sigma_1, \sigma_2, \sigma_3)\, \frac{dV}{V_o} = \sum_{i=1}^{3} \int_{V_i} n(\sigma_1, \sigma_2, \sigma_3)\, \frac{dV}{V_o} = \sum_{i=1}^{3} B_i \ , \tag{3.24}$$

where B represents the risk of event for the entire sphere while B_i represents the risk of event within volume V_i.

The probability of survival, POS, i.e., the probability that the sphere would not experience any event is

$$POS = 1 - POE \ . \tag{3.25}$$

Substituting Equation 3.14 into Equation 3.25 gives

$$POS = \exp(-B) \ . \tag{3.26}$$

Further, substituting Equation 3.24 into Equation 3.25 yields

$$POS = \exp(-B) = \exp(-\sum_{i=1}^{3} B_i) = \prod_{i=1}^{3} \exp(-B_i) = \prod_{i=1}^{3} POS_i \ , \tag{3.27}$$

where POS_i represent the POS within the individual constituent layers. The probability of an event (POE) follows as

The probability of an event (POE) follows as

$$POE = 1 - POS = 1 - \prod_{i=1}^{3} POS_i = 1 - \prod_{i=1}^{3} \exp(-B_i) = 1 - \exp\left(-\sum_{i=1}^{3} B_i\right) \ . \tag{3.28}$$

It can be seen from Equation 3.28 that the POE within the entire boulder can be computed using the risk of event corresponding to its constituents layers. This separation will be applied to boulders through the remainder of this chapter. The layer thickness is defined as diurnal skin-depth $\delta = \sqrt{\kappa P/\pi}$ with κ as the thermal diffusivity and P the diurnal period, of 24 hours.

For a boulder of volume V, made up of n concentric shells

$$B = \int_V n(\sigma_1, \sigma_2, \sigma_3)\, dV = \int_{\sum_{i=1}^{n} V_i} n(\sigma_1, \sigma_2, \sigma_3)\, dV = \sum_{i=1}^{n} \int_{V_i} n(\sigma_1, \sigma_2, \sigma_3)\, dV = \sum_{i=1}^{n} B_i \ . \tag{3.29}$$

Since each portion of the boulder's finite element model is made up of discrete finite elements, whose volume can be represented by V_e,

$$B_i = \int_{V_i} n(\sigma_1, \sigma_2, \sigma_3) dV = \int_{\sum_{e \in V_i} V_e} n(\sigma_1, \sigma_2, \sigma_3) dV = \sum_{e \in V_i} \int_{V_e} n(\sigma_1, \sigma_2, \sigma_3) dV = \sum_{e \in V_i} B_e \ , \quad (3.30)$$

where B_e represents the risk of event corresponding to a given finite element inside the boulder. The volume integral of a sufficiently smooth scalar field $F(x, y, z)$ is computed using numerical Gauss integration as

$$\int_{V_e} F(x, y, z)\, dV = \sum_{gp=1}^{8} F(x_{gp}, y_{gp}, z_{gp}) w_p J_{gp} \ , \quad (3.31)$$

where w_{gp} and J_{gp} represent the weight and the Jacobian at a Gauss point, respectively, and x_{gp}, y_{gp} and z_{gp} are its coordinates.

Combining Equations 3.29, 3.30, and 3.31 yields

$$B = \sum_{i=1}^{n} \sum_{e \in V_i} B_e = \sum_{i=1}^{n} \sum_{e \in V_i} \sum_{gp=1}^{8} n(\sigma_1, \sigma_2, \sigma_3)\Big|_{gp} w_{gp} J_{gp} \ . \quad (3.32)$$

Hence, the POE for a boulder can be expressed as

$$POE = 1 - \exp(-B) = 1 - \exp\left(- \sum_{i=1}^{n} \sum_{e \in V_i} \sum_{gp=1}^{8} n(\sigma_1, \sigma_2, \sigma_3)\Big|_{gp} w_{gp} J_{gp} \right) \ . \quad (3.33)$$

3.5 Probability of an event over time

There is insufficient experimental evidence for the identification of m and σ_o. We used $m = 15$ as was proposed by Nakamura et al. 2007 for basalt strength values and σ_o=1.0 MPa, which appears to be a reasonable threshold value for sub-critical crack growth in granites. Thus, what follows should be viewed as an index of relative probability of crack growth rather than a quantitative measure.

The tensile principal stresses obtained from all Gauss point were analyzed for boulders of different sizes to calculate the POE for different regions within the boulders. Values for POE were computed in fifteen minutes intervals throughout the day.

The probability of an event within the entire boulder is referred to $\text{POE}_{Boulder}$ and is shown in Figure 3.7. Even though the $\text{POE}_{Boulder}$ versus time follows the trend similar to that

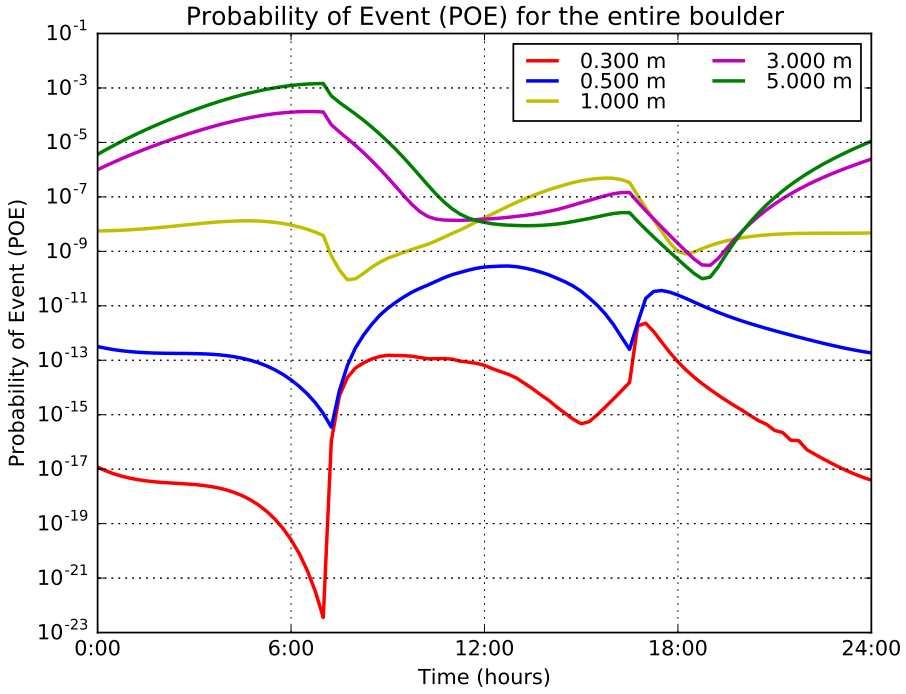

Figure 3.7: Probability of an event (POE) within the entire boulder at different times through the day

of maximum principal stress illustrated in Figure 2.19, the $\text{POE}_{Boulder}$ varies by several orders of magnitude while stress varies by less than a factor of 10. For example, the $\text{POE}_{Boulder}$ in 0.30 m diameter boulder varies between 10^{-23} and 10^{-11}, while that of 3.00 m diameter boulder varies between 10^{-9} and 10^{-4}. This contrast arises due to the difference in volume between the 0.30 m and 3.00 m diameter boulder. Even though the maximum principal stress in the 0.3 m and 0.5 m diameter boulders are similar, the $\text{POE}_{Boulder}$ between these boulders differs by up to several orders of magnitude. It can also be noted that the $\text{POE}_{Boulder}$ in 0.30 m and 0.50 m diameter boulders are similar at the time of sunrise and sunset when the magnitude of their maximum principal stresses are also similar. Even though the magnitude of maximum principal stress is similar at noon and at around 5:00 pm, $\text{POE}_{Boulder}$ for the 0.50 m diameter boulder is much higher at the noon then at 5:00 pm because the dominant tensile principal stress is spread over a larger domain at noon. Figure 2.19 further shows that even though the maximum principal stress at interior of a 1.00 m diameter boulder is

larger then that of the 3.00 m and 5.00 m diameter boulders for most part of the day, the span over which the 1.00 m diameter boulder has higher $\text{POE}_{Boulder}$ than a 3.00 m or 5.00 m diameter boulder is relatively short. The $\text{POE}_{Boulder}$ for 0.30 m diameter boulder is highest between 4:00 pm to 6:00 pm, which coincides with the time when Eppes et al. 2016 observed maximum acoustic emission activity in one boulder of about this size.

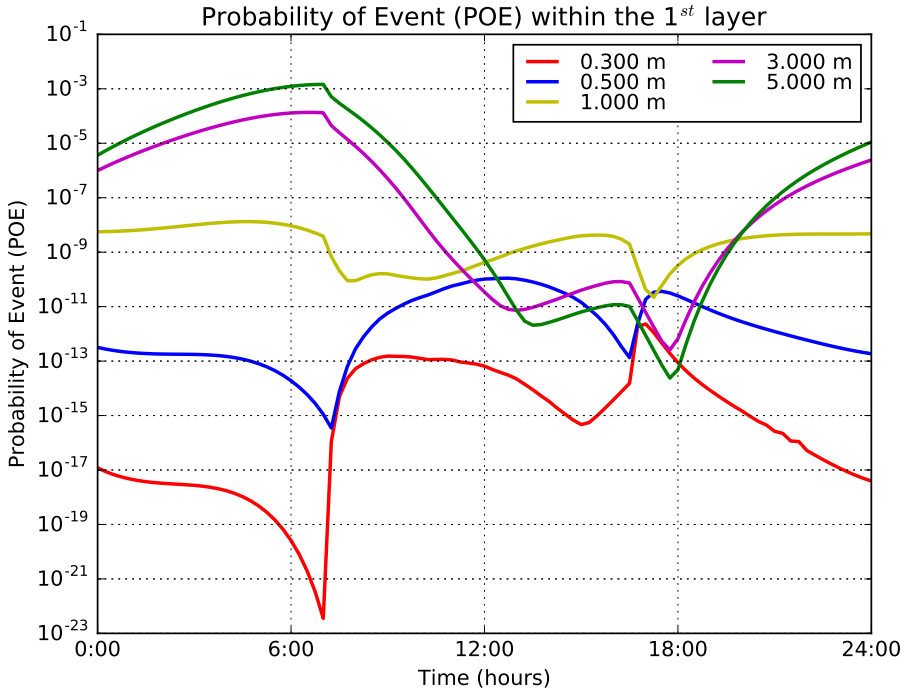

Figure 3.8: Probability of an event (POE) within one skin depth of the surface at different times through the day

Figure 3.8 illustrates the probability of event ($\text{POE}_{1^{st}layer}$) in a layer within a skin depth of the surface (1st layer in Figure 3.8). The radius of a 0.30 m diameter boulder is less than that skin depth, hence the $\text{POE}_{1^{st}layer}$ and $\text{POE}_{Boulder}$ for a 0.30 m diameter boulder are identical. The trend and order of magnitude for $\text{POE}_{1^{st}layer}$ for a 0.50 m diameter boulder is similar to POE shown in Figure 3.8. This suggests that most of the activity due to solar induced stress in a 0.50 m diameter boulder is expected in the region between the surface and skin depth. For a 1.00 m diameter boulder, the $\text{POE}_{1^{st}layer}$ and $\text{POE}_{Boulder}$ are similar throughout the night (sunset to sunrise), which coincides with the time when maximum

principal stress is dominant on the surface. $POE_{1^{st}layer}$ for 3.00 m diameter and 5.00 m diameter boulders are similar to $POE_{Boulder}$ between 7:00 pm and 10:00 am, which indicates that maximum activity during the cooling phase in these boulders happen at the region between surface and skin depth at these times. During the heating phase (daytime), POE for the interior reaches similar magnitude or, in the afternoon hours, higher magnitudes than the surface-near layer, thus reversing the trend of the cooling phase. The overall POE for larger boulders reaches a peak value toward the end of the cooling phase, while smaller boulders (less than 1.0 m) experience a peak POE in the afternoon, i.e., during the heating phase.

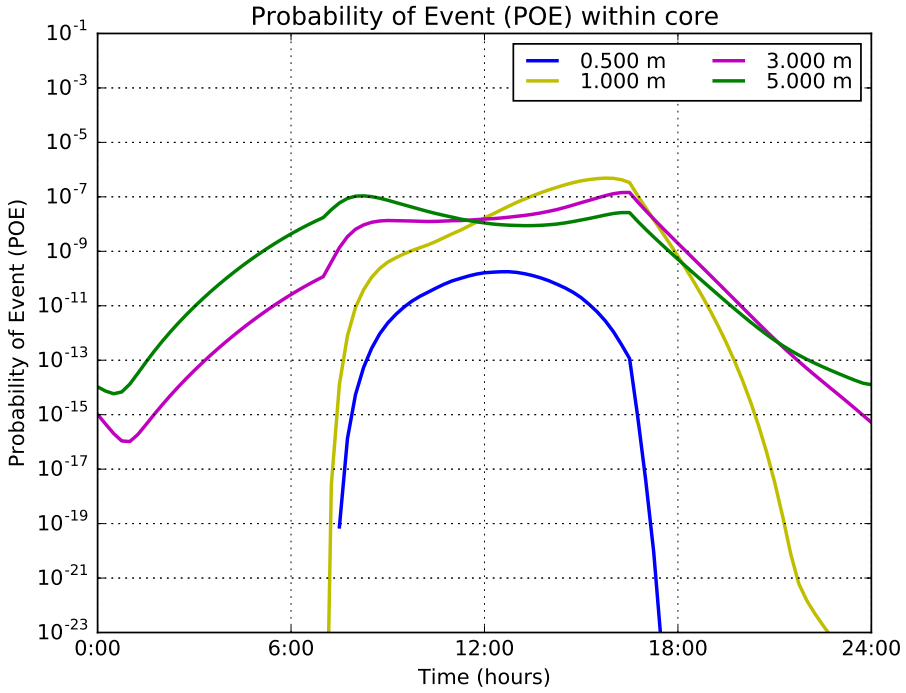

Figure 3.9: Probability of an event (POE) in the interior (>1 skin-depth from the surface)

Figure 3.9 illustrates the the probability of an event, POE_{Core}, within the core region, below one skin depth. The POE_{Core} for 1.00 m, 3.00 m, and 5.00 m diameter boulders are orders of magnitude larger than $POE_{1^{st}layer}$ during the late morning to early afternoon when the maximum principal stress is high in the boulder interior. The peak of POE_{Core} and $POE_{1^{st}layer}$ for a 0.50 m diameter boulder in the early afternoon are similar.

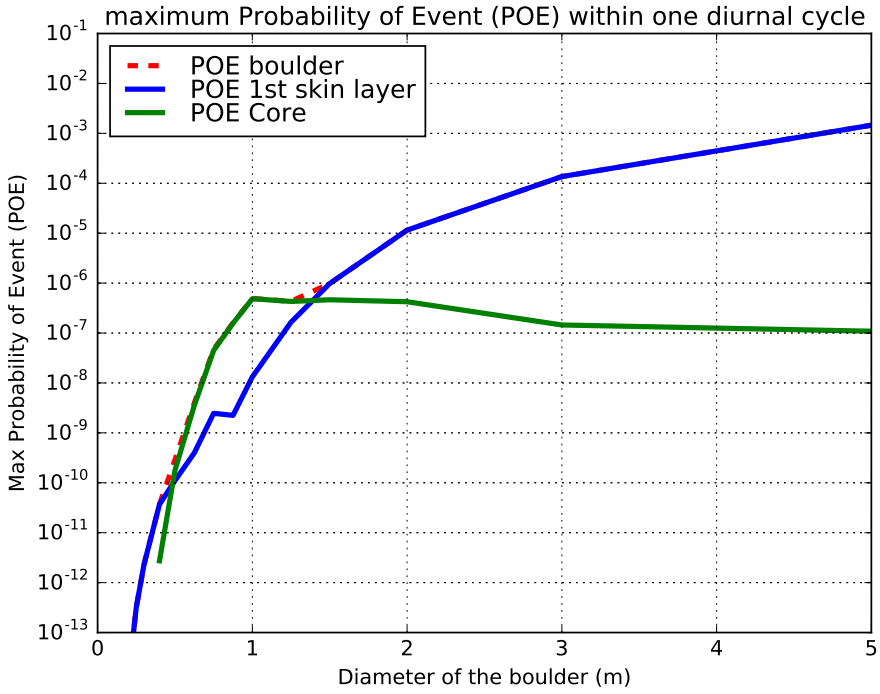

Figure 3.10: Maximum probability of an event in different sections of boulders of different sizes

Figure 3.10 illustrates the maximum POE observed in different portions of boulders for a range of sizes over a period of one day. The maximum POE is within the 1st layer for boulders less than 0.50 m or more than 1.50 m in diameter. For intermediate boulders, with diameters between 0.50 m to 1.50 m, the POE is higher within the core where tensile stresses are higher than near the surface and extend over a larger domain.

3.6 Summary and Conclusions

This chapter addresses how pre-exisiting flaws in brittle materials impacts crack growth in boulders of different diameters which are subjected to solar induced thermal stress. The focus is on quantifying the probability of a crack event (crack initiation, propagation, damage evolution, etc. detectable through acoustic emission measurements) triggered solely by solar induced tensile principal stress over different regions of the boulders at different times of the day. The principal finding is that boulders with diameters between 0.5 m to 1.5 m are more

likely to crack internally (more than one skin depth from the surface) while other boulders are more likely to crack near the surface (with one skin depth of the surface). Numerical results for a 0.3 m-diameter boulder indicated that the solar induced stresses are most likely to initiate crack growth between 4:30 pm to 6:00 pm, which is consistent with the field measurements of acoustic emissions by Eppes et al. 2016.

The study, however, was conducted with reasonable but not experimentally verified values for the Weibull parameters. Hence, this study can be improved by using the Weibull parameters obtained experimentally, and by defining the sensitivity of the results to thermal and fracture-mechanical model parameters.

Chapter 4

SUMMARY AND CONCLUSIONS

4.1 Summary

This research was conducted to develop a solid theoretical foundation for quantifying and understanding thermal stresses induced by daily exposure to the sun in boulders at the ground surface. The three dimensional, time varying temperature and stress states in spherical boulders were modeled using finite elements in MSC.marc. The model, adapted from Shi 2011 with significant improvements, was used to examine the stress state in boulder ranging in diameter from 0.15 m to 5.00 m. Taking crack growth in rocks to be dominated by tensile stresses, the magnitude of the solar induced tensile principal stresses were the natural focus of this research. The research was carried out in two stages.

The research was carried out in two parts presented in respective chapter. The first part was a systematic numerical study of the temporal 3-d distribution of solar induced temperature and maximum principal stresses in boulders of different sizes. The second part addressed the probability of crack growth caused by solar exposure in boulders of different size. It involved extraction of numerical results defining the tensile principal stresses at each Gauss point within the finite element models to calculate the probability of an event, POE, triggered solely by solar induced tensile principal stresses, which could signal crack growth in spherical boulders of different sizes. The POE was analyzed for different domains within the boulders. Our study helped us understand how the temporally varying magnitude, location and spatial extent of elevated tensile stresses collectively affect the likelihood of crack growth.

4.2 Conclusions

3d coupled thermo-mechanical simulations (Chapter 2) showed clearly how diurnal exposure to the sun affects the temperature and stress states of boulders at the ground surface for a range of boulder sizes. Tension occurs at the boulder's surface when the boulder's surface

tries to contract as the insolation decreases but faces resistance from the relatively warm interior. On the other hand, boulders experience tension in the interior when the boulder's surface tries to expand after receiving insolation but is resisted by the relatively cool interior. The interplay of the thermal and mechanical states of boulders exposed to diurnal solar radiation is strongly influenced by two length scales, the diurnal skin depth ($\delta = 0.17$ m) and the boulder size. For large boulders (diameter $> 5{-}10\,\delta$), the largest tensile stresses develop near the surface of boulders, and they increase with boulder size until they approach a limit (≈ 6.2 MPa for granite boulders). For smaller boulders, maximum tension develops inside the boulder. Its magnitude increases with diameter for diameters less than 1 m, peaks around 1 m, and decreases with size thereafter.

Section 2.3 discusses the link between size of a boulder and the size of the stressed domain. Figures 2.8, 2.10, 2.12, 2.14, and 2.16 suggest that the thickness of the stressed layer during a cooling interval is nearly independent of boulder size, suggesting a relation to the diurnal skin depth (δ) rather than radius (R). This makes the volume of the tensile domain proportional to $R^2\delta$.

The size of the tensile interior domain, as shown in Figure 2.8, appears to be proportional to boulder size, even taking on an increasing fraction of the total volume as the size increases. The volume of the interior tensile domain appears to be proportional to R^3, thus growing faster than the surface-near domain.

The probabilistic study (Chapter 3) showed that probability of an event, POE, which could lead to crack growth in spherical boulders of different diameters, followed a trend similar to that of the maximum tension experienced by the boulders at different times through the day. However, the size of the boulder strongly influenced the POE. Whereas, the POE within boulders with different sizes varied by several orders of magnitude, the maximum tensile stresses varied only by an order of magnitude. Although the magnitude of maximum principal stress at noon and around 5:00 pm for the 0.5 m diameter boulder were similar, the POE for the 0.5 m boulder was much higher at the noon because the elevated tensile stresses extended over a larger domain. Boulders smaller than 3 m experienced a higher POE after noon, while larger boulders experienced larger POE in the morning. The 0.3 m diameter boulder showed greatest likelihood of crack growth between 4:00 to 6:00 pm, which

is in accord with the period of high crack activity recorded using acoustic emissions by Eppes et al. 2016.

The probabilistic analysis of the effect of boulder size on POE shows two unexpected characteristics.

First, while the volume of the interior tensile domain grows faster with boulder size than the volume of the surface-near tensile domain, the POE grows faster for the surface-near domain and approaches a limit for the interior domain. This arises because the stress in the interior of a boulder decreases faster with increasing size than the respective domain grows, while the surface peak stress approaches a finite limit (the solution for the infinite half space).

Second, even though the stress at the center quickly decreases with boulder size (approaching zero for an infinite boulder), a domain of significant tension forms one to three skin-depths below the surface and, while tension is lower than at the surface, it suffices to generate a finite, though limited POE below the outer layer.

The probabilistic analysis merits further field validation and development, however. The analysis was based on generic Weibull parameters that are realistic and in common usage, but lack specific experimental results. Hence, this study could benefit from Weibull parameters obtained experimentally for the rock types of interest.

Last, but not least, the tools and techniques developed in this research have wide applicability in study of fracture and fatigue of brittle materials. Promising future research objectives on this subject include :

- Analyzing the direction of maximum tensile stresses throughout the boulder to find the likely direction of crack growth.

- Studying the effect of variation in latitude and longitude of the boulder's location on solar induced thermal stresses.

- Conducting a thorough sensitivity analysis of the results to thermal and fracture-mechanical model parameters.

BIBLIOGRAPHY

J. Aldred, M.C. Eppes, K. Aquino, R. Deal, J. Garbini, S. Swami, A. Tuttle, and G. Xanthos. The influence of solar-induced thermal stresses on the mechanical weathering of rocks in humid mid-latitudes. *Earth Surface Processes and Landforms*, 41(5):603–614, 2016. ISSN 10969837. doi: 10.1002/esp.3849.

T. L. Anderson. *Fracture Mechanics: Fundamentals and Applications*. Taylor & Francis Group, 2012. ISBN 0022-5096. doi: 10.1016/j.jmps.2010.02.008.

T. L. Anderson and D. Stienstra. A Model to Predict the Sources and Magnitude of Scatter in Toughness Data in the Transition Region. *Journal of Testing and Evaluation*, 17(1): 46–53, 1989.

R. Danzer, P. Supancic, J. Pascual, and T. Lube. Fracture statistics of ceramics Weibull statistics and deviations from Weibull statistics. *Engineering Fracture Mechanics*, 74(18): 2919–2932, 2007. doi: 10.1016/j.engfracmech.2006.05.028.

R. Danzer, T. Lube, P. Supancic, and R. Damani. Fracture of Ceramics. *Advanced Engineering Materials*, 10(4):275–298, 2008. doi: 10.1002/adem.200700347.

M. C. Eppes, K. Warren, S. Swami, K. Folz-Donahue, S. Evans, J. Cavendar, I. Smith, and A. Layzell. Insolation Weathering: An Instrumentation and Field Based Study (Invited). *AGU Fall Meeting Abstracts*, December 2010.

M. C. Eppes, A. Willis, J. Molaro, S. Abernathy, and B. Zhou. Cracks in Martian boulders exhibit preferred orientations that point to solar-induced thermal stress. *Nature Communications*, 6(6712):1–11, 2015. doi: 10.1038/ncomms7712.

M. C. Eppes, B. Magi, B. Hallet, E. Delmelle, P. Mackenzie-Helnwein, K. Warren, and S. Swami. Deciphering the role of solar-induced thermal stresses in rock weathering.

Bulletin of the Geological Society of America, 128(9-10):1315–1338, 2016. ISSN 19432674. doi: 10.1130/B31422.1.

A. A. Griffith. The phenomena of rupture and flow in solid. *Philosophical Transactions of the Royal Society A*, 221(582-593):163–198, 1920.

D. T. Griggs. The Factor of Fatigue in Rock Exfoliation. *The Journal of Geology*, 44(7): 783–796, 1936.

C. E. Inglis. Stresses in a plate due to the presnce of cracks and sharp corners. *Transactions of the Institute of Naval Architects*, 55:219–241, 1913. ISSN 1050-0529.

G.R. Irwin. Fracture Dynamics. In *Fracturing of Metals*, Cleveland, OH, 1948. American Society for Metals Symposium.

G.R Irwin. Onset of Fast Crack Propagation in High Strength Steel and Aluminum Alloys. Technical report, Naval Research Laboratory, Washington. D. C., 1956.

A. Jayatikala and K. Trustrum. Statistical approach to brittle fracture. *Journal of Material Science*, 12(7):1426–1430, 1977.

R. Jiang and D. N. P. Murthy. A study of Weibull shape parameter: Properties and significance. *Reliability Engineering and System Safety*, 96(12):1619–1626, 2011. ISSN 0951-8320. doi: 10.1016/j.ress.2011.09.003.

T. Lin, A. G. Evans, and R. O. Ritchie. A statistical model of brittle fracture by transgranular cleavage. *Journal of the Mechanics and Physics of Solids*, 34(5):477–497, 1986. ISSN 00225096. doi: 10.1016/0022-5096(86)90013-X.

P. Mackenzie-Helnwein. Weibull Theory in 2D and 3D. University of Washington, Seattle, WA. Personal communication, 2017.

L. D. Mcfadden, M. C. Eppes, A. R. Gillespie, and B. Hallet. Physical weathering in arid landscapes due to diurnal variation in the direction of solar heating. *Geological Society of America Bulletin*, 117(1/2):161–173, 2005. doi: 10.1130/B25508.1.

A. M. Nakamura, P. Michel, and M. Setoh. Weibull Parameters of Yakuno Basalt Targets used in Documented High-Velocity Impact Experiments. *Journal of Geophysical Research E: Planets*, 112(2):1–7, 2007. ISSN 01480227. doi: 10.1029/2006JE002757.

E. Orowan. Fracture and strength of solids. *Reports on Progress in Physics*, 12(1):185–232, 1949.

J. Petrovic. Weibull statistical fracture theory for the fracture of ceramics. *Metallurgical Transactions A*, 18(11):1829–1834, 1987. ISSN 03602133. doi: 10.1007/BF02647012.

J. Shi. Study of Thermal Stresses in Rocks Due to Diurnal Solar Exposure Jian. Master's thesis, University of Washington, 2011.

M. Thomas, J. D. A. Clarke, and C. F. Pain. Weathering, Erosion and Landscape Processes on Mars Identified from Recent Rover Imagery, and Possible Earth Analogues. *Australian Journal of Earth Sciences*, 52(3):365–378, 2005. doi: 10.1080/08120090500134597.

W. Weibull. A Statistical Theory of the Strength of Materials. *Ingeniorsvetenskap sakademiens*, 151:1–45, 1939.

W. Weibull. A statistical distribution function of wide applicability. *Journal of applied mechanics*, 18:293–297, 1951.

T. Yokoyama and Y. Matsukura. Field and laboratory experiments on weathering rates of granodiorite : Separation of chemical and physical processes. *Geology*, 24(10):809–812, 2006. doi: 10.1130/G22625.1.